

Spin-dependent sub-GeV Inelastic Dark Matter-electron scattering and Migdal effect: (I). Velocity Independent Operator

Jiwei Li,^{1,*} Liangliang Su,^{1,†} Lei Wu,^{1,‡} and Bin Zhu^{2,§}

¹*Department of Physics and Institute of Theoretical Physics,
Nanjing Normal University, Nanjing, 210023, China*

²*Department of Physics, Yantai University, Yantai 264005, China*

Abstract

The ionization signal provide an important avenue of detecting light dark matter. In this work, we consider the sub-GeV inelastic dark matter and use the non-relativistic effective field theory (NR-EFT) to derive the constraints on the spin-dependent DM-electron scattering and DM-nucleus Migdal scattering. Since the recoil electron spectrum of sub-GeV DM is sensitive to tails of galactic DM velocity distributions, we also compare the bounds on corresponding scattering cross sections in Tsallis, Empirical and standard halo models. With the XENON1T data, we find that the exclusion limits of the DM-proton/neutron and DM-electron scattering cross sections for exothermic inelastic DM are much stronger than those for the endothermic inelastic DM. Each limits of the endothermic inelastic DM can differ by an order of magnitude at most in three considered DM velocity distributions.

* ljw@njnu.edu.cn

† liangliangsu@njnu.edu.cn

‡ leiwu@njnu.edu.cn

§ zhubin@mail.nankai.edu.cn

CONTENTS

I. Introduction	3
II. Dark Matter Velocity Distribution Function	4
III. Inelastic Dark Matter-Nucleus Migdal Scattering	7
A. Calculations	8
B. Numerical Results and Discussions	16
IV. Inelastic Dark Matter-Electron Scattering	22
A. Calculations	23
B. Numerical Results and Discussions	25
V. Conclusion	28
VI. Acknowledgements	30
References	30

I. INTRODUCTION

Numerous astronomical and cosmological observations have provided evidence for the existence of dark matter (DM) in the universe. However, besides its gravitational interaction, other physical properties of DM remain mystery. From the perspective of particle physics, dark matter may be made up of a hypothetical particle that is still undetected. Among the various conjectures, the weakly interacting massive particles (WIMPs) have been widely studied in the various experiments.

Direct detection that attempts to discern signals induced by DM at extremely low backgrounds has made great efforts in the past few years [1–13]. However, there is no any evidence of WIMP dark matter in the typical mass range. This strongly motivates the search for sub-GeV dark matter [9–32]. While the low momentum transfer of sub-GeV DM can not produce the observable nuclear recoil signal in the conventional detectors. With the improvements of direct detection experiments, we can access to the low mass DM by using the ionization events. Such signals can arise from the scattering of electrons with DM [5, 10–14, 18, 19, 27–35], and the secondary effects in the DM-nuclear interactions, such as the Migdal scattering [9, 20–26, 36–41].

In this paper, we will study the ionization signals of sub-GeV inelastic dark matter (iDM), including Migdal effect and DM-electron scattering. Although originally proposed as an explanation for the DAMA anomaly, models of iDM that contain DM with a ground and an excited state represent a viable and compelling paradigm for light thermal DM [42–55]. Given the current strong constraints on the spin-independent (SI) cross section, we calculate the spin-dependent (SD) iDM-nucleus/electron scattering. We consider the operator $\mathbf{O}_4 = \vec{\mathbf{S}}_\chi \cdot \vec{\mathbf{S}}_\mathcal{N}$; this type of SD interaction is the only one in the leading order that is not suppressed by momentum transfer. The SD interactions can even become the only interactions available in direct detection experiments, such as models with light pseudoscalar mediators [56]. For other models, the SD interaction may still dominate, e.g. the scattering cross section for a Dirac DM particle interacting through its anomalous magnetic dipole moment, where the SD-like part (dipole-dipole) dominates in certain parameter space [57]. Or when the DM is the Majorana fermion or a real vector boson, the SD interaction can naturally dominate (but is not always guaranteed) [58]. In the future, if a signal associated with SD is observed, it will rule out the spinless DM particles by and large.

On the other hand, the velocity distribution function (VDF) of the local DM halo can have a non-negligible impact on the direct detection [59–62]. In particular, the electron recoil spectrum is sensitive to the high-velocity tail of the DM halo. As a benchmark distribution, the Standard Halo Model (SHM) is usually adopted [63], however, it still can not accurately describe the distribution of DM in the Galaxy [64]. This motivates other alternative halo models for the VDF [65], such as Tsallis and Empirical models. We will also discuss their impacts on the exclusion limits of iDM-nucleus/electron scattering.

The paper is structured as follows. In Sec. II, we compare the velocity distribution functions for three models: the Standard Halo Model, the Tsallis model and the empirical model. In Sec. III and Sec. IV, we investigate the ionization rates of the spin-dependent scattering of the inelastic dark matter with the nucleus and the electron targets, respectively. With the available data, we obtain the exclusion limit for spin-dependent inelastic dark matter-nucleus Migdal/electron scattering in three velocity distribution models. Finally, we draw the conclusions in Sec. V.

II. DARK MATTER VELOCITY DISTRIBUTION FUNCTION

In the DM direct detections, the astrophysical properties of the local DM halo distribution, such as local DM density, mean DM velocity, etc., can significantly change the sensitivity. In particular, the electron spectrum is exceptionally sensitive to the high-velocity tail of the local velocity distribution of dark matter [65]. The most popular and widely used standard halo model (SHM) in DM direct detection experimental analysis, which assumes DM particles are in an isothermal sphere and obey the isotropic Maxwell-Boltzmann velocity distribution function (VDF). Although its simple analytical form is appealing [64], this model cannot adequately explain the distribution of DM particles in the Galaxy. Consequently, it is important to investigate different velocity distribution models to substitute for the halo model. Based on the work in Ref. [65], this paper also introduces two additional velocity distribution models: Tsallis Model and an Empirical Model. We will discuss the effects on DM-Target scattering caused by different VDF models.

In the rest frame of the Galaxy, the SHM is given by

$$f_{\text{SHM}}(\vec{v}) \propto \begin{cases} e^{-|\vec{v}|^2/v_0^2} & |\vec{v}| \leq v_{\text{esc}} \\ 0 & |\vec{v}| > v_{\text{esc}}. \end{cases} \quad (1)$$

The escape speed of the galaxy limits the speed of DM particles gravitationally bound to our galaxy, so a physical cut-off point is set at the local escape speed v_{esc} , with v_0 as the circular velocity at the Solar position [59]. The rotation curve in this model will be asymptotically flat at large r (i.e. the distance from the centre of the Galaxy), and v_0 is usually regarded as the value of the curve at this point. In the laboratory frame it has the following analytical forms

$$f_{\text{SHM}}(\vec{v}) = \frac{1}{K} e^{-|\vec{v} + \vec{v}_E|^2/v_0^2} \Theta(v_{\text{esc}} - |\vec{v} + \vec{v}_E|), \quad (2)$$

The velocity distribution of the SHM is truncated at the escape speed v_{esc} through the Heaviside function Θ , with the normalization coefficient

$$K = v_0^3 \left(\pi^{\frac{3}{2}} \text{Erf}\left(\frac{v_{\text{esc}}}{v_0}\right) - 2\pi \frac{v_{\text{esc}}}{v_0} \exp\left(-\frac{v_{\text{esc}}^2}{v_0^2}\right) \right) \quad (3)$$

that results from $\int f(\vec{v}) d^3\vec{v} = 1$.

The features of the local VDFs derived from DM cosmological simulations that include baryonic physics are largely consistent with the SHM; however, several studies [59, 65–69] using data from DM-only simulations reveal a significant deviation from the overall trends manifested by the relevant local VDFs compared to the SHM. These simulations show that, especially in the high-velocity tail of the distribution, different features with the SHM will appear. One point worth making is that although adding baryons to the simulation makes the process more complex, it is nevertheless essential to restore the possible real universe.

Next, we discuss some alternative models in which the VDF of the Tsallis Model (Tsa) [70] can be considered more compatible with the numerical results of N –*body* simulations that include baryons [71, 72]. According to the statistical results of Tsallis, the definition of standard Boltzmann-Gibbs entropy is extended by introducing the entropy index q_s , as following

$$\begin{aligned} S_{q_s} &\equiv \frac{k}{q_s - 1} \sum_{i=1} p_i (1 - p_i^{q_s-1}) \\ &= -k \sum_i p_i^{q_s} \ln_{q_s} p_i, \end{aligned} \quad (4)$$

where p_i is the probability for a particle to be in state i , and $\ln_{q_s} p = (p^{1-q_s} - 1)/(1 - q_s)$. Note that q_s is an arbitrary positive real number and that Eq. 4 recovers the standard Boltzmann-Gibbs entropy expression when the limit $q_s \rightarrow 1$. Then, we can write down the velocity distribution function according to this Tsallis entropy

$$f_{\text{Tsa}}(\vec{v}) \propto \begin{cases} \left[1 - (1 - q_s) \frac{\vec{v}^2}{v_0^2} \right]^{1/(1-q_s)} & |\vec{v}| < v_{\text{esc}} \\ 0 & |\vec{v}| \geq v_{\text{esc}}. \end{cases} \quad (5)$$

In this paper, we take $q_s = 0.813$ [65] to calculate our results. It is advantageous to use the Tsa model to elucidate the velocity distribution of the DM halo because the escape speed is already physically involved in the range $q_s < 1$, determined by $v_{\text{esc}} = v_0^2/(1 - q_s)$, without the need for manual truncation, but the escape speed still needs to be set for $q_s > 1$. Finally,

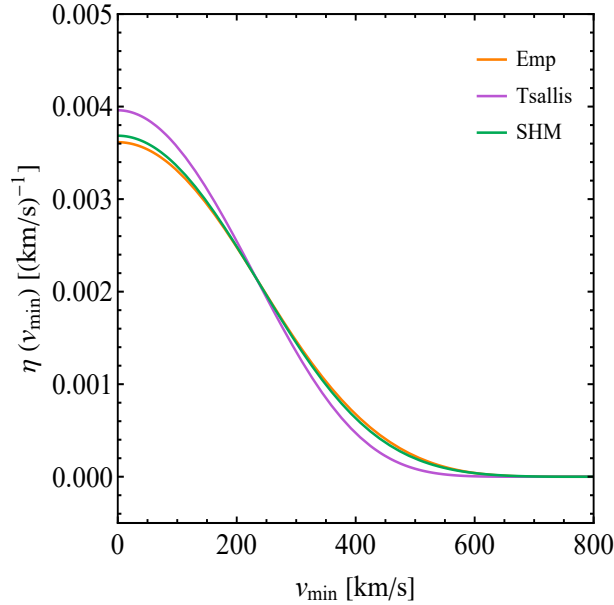


FIG. 1. The $\eta(v_{\min})$ is derived after integration over the velocity distribution, which varies with the parameters of the three models. For fixed the astrophysical parameters $v_0 = 228.6$ km/s, $v_E = 232$ km/s and $v_0 = 528$ km/s, the orange line represents the Empirical model ($p = 1.5$), the green represents the Standard Halo Model and the purple represents the Tsallis model ($q_s = 0.813$).

based on the work of Ref. [65, 69, 73] another alternative model we introduce is an empirical model (Emp). It is derived from Hydrodynamical simulations with baryons on the data of DM-only cosmological simulation [74, 75]. In the Galactic rest frame, the empirical model

described has a velocity distribution of the following form

$$f_{\text{Emp}}(\vec{v}) \propto \begin{cases} \exp\left(-\frac{|\vec{v}|}{v_0}\right) (v_{\text{esc}}^2 - |\vec{v}|^2)^p & |\vec{v}| < v_{\text{esc}} \\ 0 & |\vec{v}| \geq v_{\text{esc}}. \end{cases} \quad (6)$$

This empirical model is an exponential-based distribution, where p is an adjustable parameter, and following the best-fit parameters for the Eris simulations [65, 76], $p = 1.5$ is set as our fiducial model. The shape of the VDF for this empirical model primarily relies on a proportional relationship, r/r_s , the ratio of the VDF's measured radius to the scaled radius of the halo density profile, and the uncertainty of the VDF is also derived from this quantity [69].

In Fig. 1, we have depicted with solid lines of various colours the $\eta(v_{\text{min}})$ resulting from the three velocity distribution models after integral $\eta(v_{\text{min}}) = \int \frac{d^3\vec{v}}{|\vec{v}|} f_{\chi}(\vec{v}) \Theta(|\vec{v}| - v_{\text{min}})$. v_{min} is the minimum incoming DM velocity that causes nuclear recoil, and we will discuss it in the next section. Here we have adopted the suggested astrophysical parameters, $v_0 = 228.6 \text{ km/s}$ [77], $v_E = 232 \text{ km/s}$ [78] and $v_0 = 528 \text{ km/s}$ [79], to show the shape of $\eta(v_{\text{min}})$ under different models. It can be observed that as the speed of DM shifts from low to high, the $\eta(v_{\text{min}})$ transition in the Empirical model and the Standard Halo Model appears to be smoother, whereas the $\eta(v_{\text{min}})$ of the Tsallis model is steeper than the other two models. In the low speed region, the $\eta(v_{\text{min}})$ of the Emp and SHM diverge, although not significant (Tsa's diverges most from both). However as the DM speed increase, the Emp curve almost coincides with that of SHM.

In the following discussion, we turn our attention to inelastic dark matter-nucleus Migdal scattering and inelastic dark matter-electron scattering. We will examine the impact of the velocity distribution model discussed above through the electron spectrum induced by these two processes.

III. INELASTIC DARK MATTER-NUCLEUS MIGDAL SCATTERING

We introduce a fermion dark matter χ with spin 1/2 coupling to a Standard Model (SM) particle \mathcal{N} . Assuming inelastic scattering between them, $\chi\mathcal{N} \rightarrow \chi'\mathcal{N}$, mass splitting $\delta = m_{\chi'} - m_{\chi}$ occurs between the incoming and outgoing dark matter (more details on kinematics are discussed below). If we consider that their interaction is via axial-vector-

axial-vector couplings, the Lagrangian density \mathcal{L} at low momentum transfer is

$$\mathcal{L}_{\text{int}} \supset \bar{\chi}' \gamma^\mu \gamma^5 \chi \bar{\mathcal{N}} \gamma_\mu \gamma^5 \mathcal{N}. \quad (7)$$

This is called the standard spin-dependent interaction in non-relativistic effective field theory (NR-EFT) and is usually reduced to the type of the two spin operators, $-4\vec{\mathbb{S}}_\chi \cdot \vec{\mathbb{S}}_{\mathcal{N}} = -4\mathbf{O}_4$. Such a spin-dependent interaction is the only one in the leading order that is not suppressed by momentum transfer. This may allow us to place stronger constraints on the DM-nucleus scattering of SD interactions.

A. Calculations

We begin with the perspective of inelastic dark matter-nucleon scattering kinematics. In general, there are two different ways to reveal inelasticity [57], DM particle of mass m_χ undergo mass splitting after scattering with nucleus become to $m_{\chi'} - m_\chi = \delta$, or there is the possibility of the nucleon transitioning from a low-energy state to an excited state. The latter case has been studied in many literatures [80–86], and for the sake of simplicity we do not consider this possibility in this work.

We focus on the process $\chi(\vec{p}) + N(\vec{k}) \rightarrow \chi'(\vec{p}') + N(\vec{k}')$, where χ and χ' are dark matter particles in the initial and final states, respectively, and N is a nucleon. For non-relativistic limit, inspired by the conservation of energy in the center-of-mass (CM) framework we have

$$\begin{aligned} \frac{1}{2}\mu_N v^2 &= \frac{p'^2}{2m_{\chi'}} + \frac{k'^2}{2m_N} + \Delta \\ &= \frac{(\vec{p} + \vec{q})^2}{2m_{\chi'}} + \frac{(\vec{k} - \vec{q})^2}{2m_N} + \Delta, \end{aligned} \quad (8)$$

where $\mu_N = \frac{m_\chi m_N}{(m_\chi + m_N)}$ is the reduced mass of the initial $\chi - N$ system, $\vec{v} \equiv \frac{\vec{p}}{m_\chi} - \frac{\vec{k}}{m_N}$ is the relative velocity between the DM particle and the nucleon. The momentum transfer $\vec{q} \equiv \vec{p}' - \vec{p} = \vec{k} - \vec{k}'$. It should be noted that the momentum transfer \vec{q} is approximately Galilean invariant in the inelastic scattering under NR boost when the mass splitting $|\delta| \ll m_\chi$. Δ shows the initial kinetic energy lost due to inelastic effects. To better discuss the Migdal effect and electron scattering that follow, we write Δ here as $\Delta = E_{\text{em}} + \delta$ (for nucleus scattering, $\Delta = \delta$), and E_{em} is the electromagnetic energy available to excite the electron. In this paper we have conventionally defined that $\delta > 0$ corresponds to the endothermic

scattering, while $\delta < 0$ is the exothermic scattering. Comparing the Δ with initial kinetic energy E_{kin} of the system, $\Delta = 0$ corresponds to the usual elastic scattering. Apparently, we can know from Eq. 8 that the maximum possible value of Δ for the scattering should be equal to the initial available kinetic energy

$$E_{\text{kin}} \equiv \frac{1}{2}\mu_N v^2 = \Delta_{\text{max}}. \quad (9)$$

Significantly, the masses of DM and nucleons are so large compared to kinetic energy that scattering is only kinematically allowed in the $|\Delta| \ll m_\chi$ scenario.

To facilitate our calculations, we set $\vec{p}_i \equiv \mu_N \vec{v}$ for initial system momentum, and in the final system $\chi' - N$, we can write $E_f = \frac{1}{2}\mu' v'^2 + \Delta$. In the NR limit approximation, we will take $\Delta/\mu_N^{(i)}$ as a parameter of order $\mathcal{O}(v^2)$, thus we have

$$v'^2 = v^2 - 2\frac{\Delta}{\mu_N} \quad (10)$$

and the square of the momentum of the final system $p_f'^2$

$$p_f'^2 = \mu_N'^2 v'^2 \simeq \mu_N^2 v^2 - 2\mu_N \Delta. \quad (11)$$

The transfer momentum $\vec{q} = (\vec{p}_f' - \vec{p}_i)$ is the same in both frames, so that we then can express the atomic recoil energy in the frame of the detector as

$$E_R = \frac{\mu_N^2 v^2}{m_N} \left(1 - \cos \theta \sqrt{1 - \frac{2\Delta}{\mu_N v^2}} \right) - \frac{\mu_N \Delta}{m_N}, \quad (12)$$

where θ is the DM-nucleon scattering angle in the CM frame. It is worth mentioning that the derivation above for $\mu_N \sim \mathcal{O}(\text{GeV})$, if $\Delta \sim \mathcal{O}(\text{keV})$, there is $\mu_N \simeq \mu_N' = m_\chi' m_N / (m_\chi' + m_N)$. But in numerical calculation, we still maintain the complete expansion ($\mu_N \neq \mu_N'$).

We can also see from the Eq. 12 that if the incoming DM has a fixed speed, there will be a maximum E_R^{max} and a minimum E_R^{min} of the recoil energy, corresponding to $\theta = \pi$ and 0, respectively. Likewise, when the DM particle imparts a given recoil energy to the target nucleus, the incident speed of DM is kinematically limited. If we express the momentum transfer $q = \sqrt{2m_N E_R}$ in terms of energy recoil, then we get the minimum DM velocity that can cause nuclear recoil,

$$v_{\text{min}}(E_R) = \left| \frac{q}{2\mu_N} + \frac{\Delta}{q} \right| = \frac{1}{\mu_N \sqrt{2m_N E_R}} |m_N E_R + \mu_N \Delta|. \quad (13)$$

Next, we will introduce a non-relativistic effective field theory to help us discuss inelastic dark matter-nucleus scattering. Given the average velocity of DM in the galactic halo is $v \sim \mathcal{O}(10^{-3})$, the non-relativistic effective field theory provides a bottom-up framework to study the DM direction detection [25, 87–93]. This formalism enables the decomposition of the interaction of dark matter with the nucleus into two classes of response functions. And it allows us to use pre-calculated nuclear form factors for the relevant interaction operators.

According to the work of Haxton et al. [88–90], they established an EFT based on elastic DM-nucleus scattering. This approach allows to construct a series of effective operators from four Galilean invariants: the DM particle spin \vec{S}_χ , nucleon spin \vec{S}_N , the momentum transfer $i\vec{q}$ and the transverse velocity $\vec{v}_{el}^\perp \equiv \vec{v} + \frac{\vec{q}}{2\mu_N}$. However, in the case of inelastic scattering, it is necessary to modify the quantity due to mass splitting. As indicated by the formalism in the Ref. [94], the NR-EFT for inelastic scattering of dark matter is a direct extension of elastic scattering. It pointed out in the context that at the leading order of the v expansion, the only modification made is that \vec{v}_{el}^\perp changed from elastic scattering. According to the kinematics of inelastic scattering, the mass splitting δ allows for a contribution to the incident velocity component perpendicular to the momentum transfer \vec{q} , so that a new Galilean invariant on inelastic scattering can be obtained by adding a new component for modification

$$\vec{v}_{el}^\perp \rightarrow \vec{v}_{inel}^\perp \equiv \vec{v} + \frac{\vec{q}}{2\mu_N} + \frac{\Delta}{|\vec{q}|^2} \vec{q}. \quad (14)$$

The above equation satisfies $\vec{q} \cdot \vec{v}_{inel}^\perp = 0$ due to the conservation of energy. The effect of this inelasticity will be directly reflected in the DM particle response function $\mathcal{R}_X^{\tau\tau'}$ rather than the nucleon response function $\mathcal{W}_X^{\tau\tau'}$. However, we are concerned with the effective spin-dependent operator $\mathbf{O}_4 = \vec{S}_\chi \cdot \vec{S}_N$, which does not depend on \vec{v}_{inel}^\perp . In other words, for our calculations we can still make use of the nucleon matrix elements from Ref. [90].

For a given Lagrangian, the invariant amplitude of the DM-nucleon can be obtained using spherical harmonics and multipole expansions,

$$\begin{aligned} \mathcal{M} &= \sum_{\tau=0,1} \langle j'_\chi, M'_\chi; j'_N, M'_N | \mathbf{O}_{JM;\tau}(q) | j_\chi, M_\chi; j_N, M_N \rangle \\ &\equiv \sum_{\tau=0,1} \langle j'_\chi, M'_\chi; j'_N, M'_N | \sum_{i=1}^A \mathbf{O}_{JM}(q\vec{x}_i) t^\tau(i) | j_\chi, M_\chi; j_N, M_N \rangle. \end{aligned} \quad (15)$$

Here $\mathbf{O}_{JM;\tau}(q)$ contains six operators familiar to the standard model electroweak interaction theory: \mathbf{M} , $\mathbf{\Sigma}'$, $\mathbf{\Delta}$, $\mathbf{\Sigma}''$, $\mathbf{\Phi}''$, $\mathbf{\tilde{\Phi}}'$. This is the result obtained by considering only elastic

transitions and assuming that the nuclear ground state obeys CP and parity conservation. According to semi-leptonic electroweak theory [95–97], the only spin-dependent interactions of interest to us are only two related single particle operators, Σ' and Σ'' , corresponding to axial transverse and axial longitudinal operators, respectively,

$$\begin{aligned}\Sigma'_{JM;\tau}(q^2) &\equiv -i \sum_{i=1}^A \left\{ \frac{1}{q} \vec{\nabla}_i \times \vec{M}_{JJ}^M(q\vec{x}_i) \right\} \cdot \vec{\sigma}(i) \tau_3(i) \\ \Sigma''_{JM;\tau}(q^2) &\equiv \sum_{i=1}^A \left\{ \frac{1}{q} \vec{\nabla}_i \cdot \vec{M}_{JM}(q\vec{x}_i) \right\} \cdot \vec{\sigma}(i) \tau_3(i).\end{aligned}\tag{16}$$

By averaging over initial spins and summing over outgoing spins, we then write down the DM-nucleus scattering transition probability,

$$\begin{aligned}P_{tot} &= \frac{1}{2j_\chi + 1} \frac{1}{2j_N + 1} \sum_{\text{spins}} |\mathcal{M}|^2 \\ &= \frac{4\pi}{2j_N + 1} \sum_{\tau=0,1} \sum_{\tau'=0,1} \left[\mathcal{R}_{\Sigma''}^{\tau\tau'} \left(\vec{v}_{T_{inel}}^{\perp 2}, \frac{\vec{q}^2}{m_N^2} \right) \mathcal{W}_{\Sigma''}^{\tau\tau'}(q^2) + \mathcal{R}_{\Sigma'}^{\tau\tau'} \left(\vec{v}_{T_{inel}}^{\perp 2}, \frac{\vec{q}^2}{m_N^2} \right) \mathcal{W}_{\Sigma'}^{\tau\tau'}(q^2) \right],\end{aligned}\tag{17}$$

where j_χ and j_N label the dark matter and nuclear spin, respectively. The Eq. 17 expresses the transition probability as the product of the DM particle response functions $\mathcal{R}_X^{\tau\tau'}$ and nuclear response functions $\mathcal{W}_X^{\tau\tau'}$. The former is determined by the bilinear functions c_i^τ 's in the EFT coefficients, which distinguishes particle physics well from nuclear physics. In the isospin basis $c_i^{\tau(\prime)}$, here we list the DM particle response functions considered,

$$\begin{aligned}\mathcal{R}_{\Sigma'}^{\tau\tau'} \left(\vec{v}_{T_{inel}}^{\perp 2}, \frac{\vec{q}^2}{m_N^2} \right) &= \frac{1}{8} \left[\frac{\vec{q}^2}{m_N^2} \vec{v}_{T_{inel}}^{\perp 2} c_3^\tau c_3^{\tau'} + \vec{v}_{T_{inel}}^{\perp 2} c_7^\tau c_7^{\tau'} \right] + \frac{j_\chi(j_\chi + 1)}{12} \left[c_4^\tau c_4^{\tau'} \right. \\ &\quad \left. + \frac{\vec{q}^2}{m_N^2} c_9^\tau c_9^{\tau'} + \frac{\vec{v}_{T_{inel}}^{\perp 2}}{2} \left(c_{12}^\tau - \frac{\vec{q}^2}{m_N^2} c_{15}^\tau \right) \left(c_{12}^{\tau'} - \frac{\vec{q}^2}{m_N^2} c_{15}^{\tau'} \right) + \frac{\vec{q}^2}{2m_N^2} \vec{v}_{T_{inel}}^{\perp 2} c_{14}^\tau c_{14}^{\tau'} \right] \\ \mathcal{R}_{\Sigma''}^{\tau\tau'} \left(\vec{v}_{T_{inel}}^{\perp 2}, \frac{\vec{q}^2}{m_N^2} \right) &= \frac{\vec{q}^2}{4m_N^2} c_{10}^\tau c_{10}^{\tau'} + \frac{j_\chi(j_\chi + 1)}{12} \left[c_4^\tau c_4^{\tau'} \right. \\ &\quad \left. + \frac{\vec{q}^2}{m_N^2} \left(c_4^\tau c_6^{\tau'} + c_6^\tau c_4^{\tau'} \right) + \frac{\vec{q}^4}{m_N^4} c_6^\tau c_6^{\tau'} + \vec{v}_{T_{inel}}^{\perp 2} c_{12}^\tau c_{12}^{\tau'} + \frac{\vec{q}^2}{m_N^2} \vec{v}_{T_{inel}}^{\perp 2} c_{13}^\tau c_{13}^{\tau'} \right].\end{aligned}\tag{18}$$

The nuclear response functions $\mathcal{W}_X^{\tau\tau'}$, obtained by multipoles expansion and summing over

the nuclear states,

$$\begin{aligned}\mathcal{W}_{\Sigma''}^{\tau\tau'}(q^2) &= \sum_{J=1,3,\dots}^{\infty} \langle j_N \| \Sigma''_{J;\tau}(q) \| j_N \rangle \langle j_N \| \Sigma''_{J;\tau'}(q) \| j_N \rangle \\ \mathcal{W}_{\Sigma'}^{\tau\tau'}(q^2) &= \sum_{J=1,3,\dots}^{\infty} \langle j_N \| \Sigma'_{J;\tau}(q) \| j_N \rangle \langle j_N \| \Sigma'_{J;\tau'}(q) \| j_N \rangle\end{aligned}\tag{19}$$

where $\mathcal{W}_{\Sigma'}^{\tau\tau'}$ and $\mathcal{W}_{\Sigma''}^{\tau\tau'}$ only receive contributions from the odd multipoles. A more complete formulation of Eq. 17, Eq. 18 and Eq. 19 is shown in the Ref. [90]. The full amplitude or the nuclear responses can be calculated using the *Mathematica* package *DMFormFactor* given in the text. Notice that, relativistic normalisation is used in Eq. 17 to produce a dimensionless $|\mathcal{M}|^2$, which is achieved by multiplying by a factor of $(4m_\chi m_T)^2$. From the transition probability P_{tot} , one can immediately obtain the differential cross section

$$\frac{d\sigma}{dE_R} = \frac{2m_T}{4\pi v^2} \left[\frac{1}{2j_\chi + 1} \frac{1}{2j_N + 1} \sum_{\text{spins}} |\mathcal{M}|^2 \right].\tag{20}$$

Next, we turn our attention to the Migdal effect of iDM-nucleus scattering. Based on the work in Ref. [31, 36–40, 98, 99], we will briefly review the Migdal effect and present the main formulas to facilitate our calculation of the scattering cross section. The Migdal effect is the process of atomic ionization or excitation. In the scattering of DM particles and nuclear, the nucleus suddenly receives a transfer momentum \vec{q} , and the electron cloud cannot ‘catch up’ instantaneously, which makes it possible to detect the subsequent electromagnetic signatures. Thus, the theoretical calculation of the Migdal effect and the DM-electron scattering rate is closely related.

Kinematically, Migdal and electron scattering are identical: the initial state is a DM particle with a bound atom, and the final state is a DM particle with an ionized atom and an unbound electron. To demonstrate the physical process of Migdal, following Ref. [36], it is assumed that both the incoming and outgoing DM are plane waves. However, the outgoing atom is regarded as an atom in an excited state, where the ionized electrons belong to the continuum of the atomic Hamiltonian [99]. In this formalism, treating the nucleus and electron as a single many-particle system would allow us to treat the transfer momentum \vec{q} as originating from the DM rather than other specific components. According to the conservation of energy in Eq. 8, we have

$$E_{\text{em}} = \vec{q} \cdot \vec{v} + \frac{q^2}{2\mu_N} - \delta,\tag{21}$$

where $E_{\text{em}} = E_{e,f} - E_{e,i}$ is the transfer energy available for scattered electrons. There exists a maximum value of E_{em} , which can be derived from Eq. 9,

$$E_{\text{em}}^{\text{max}} \simeq \frac{1}{2} m_\chi v_{\text{max}}^2 - \delta, \quad (22)$$

where assumed $m_\chi \ll m_N$, v_{max} is the maximum DM incoming velocity (in laboratory frame). This indicates that the maximum value $E_{\text{em}}^{\text{max}}$ is not related to the initial occupied energy level of Migdal electrons and target nucleus. We would like to point out that these inelastic effects mainly affect in kinematics.

Nevertheless, the dynamics of Migdal and electron scattering differ significantly depending on whether the DM interacts directly with electrons or the nucleus. To clarify their connection, we briefly review the process from isolated atom reduction to nuclear recoil and projection onto the electron cloud [36]. In the relativistic limit, we convert the dark matter-nucleus interaction into an interaction potential V_{int} , then the total Hamiltonian for the atom can be written as

$$H_{\text{tot}} = H_A + \frac{\hat{p}_\chi^2}{2m_\chi} + V_{\text{int}}(\vec{x}_N - \vec{x}_\chi), \quad (23)$$

where \vec{x}_N and \vec{x}_χ represent the positional operators of nucleus and DM, and H_A is the approximate Hamiltonian of the atomic system. Therefore, the elements of the transition matrix are derived by using reduced atomic eigenstates of H_{tot}

$$iT_{FI} \sim F(q_N^2) \times \mathcal{M}(q_N^2) \times Z_{FI}(q_e) \times i(2\pi)^4 \delta^4(p_F - p_I). \quad (24)$$

Here T_{FI} is decomposed into the nuclear form factor $F(q_N^2)$ and the DM-nucleon scattering invariant matrix element $\mathcal{M}(q_N^2)$, both evaluate the interaction of nucleons. And the factor Z_{FI} associated with the electron cloud transition. This treatment makes explicit the conservation of momentum-energy at invariant amplitude.

Notice that Eq. 24 assumes that the initial state of atoms in the laboratory frame are stationary, i.e. $\vec{v}_I = 0$. Moreover, V_{int} is the interaction potential between the nucleus and the DM, it does not contain the position operator \vec{x} of the electron, so theoretically, the electron cannot be induced to transition. Assume that momentum \vec{q} is transferred instantaneously to the nucleus, in which case the entire atom suddenly obtains velocity $\vec{v}_A \equiv \frac{\vec{q}_e}{m_e}$ and leaves its stationary electrostatic potential. At this moment the wave function of the electron of the moving atom will change, considering $\vec{q}_e \equiv \frac{m_e}{m_N} \vec{q}$ as the effective momentum of the electron.

Following the method of Ref. [36], where electron transitions and nucleon scattering are linked to construct the approximate energy eigenstates of the moving atoms by applying the Galilean transformation with the velocity parameter \vec{v}_A . In other words, the wave function of the atomic final state is composed of the eigenstate of the atom at rest multiplied by the phase factor $e^{i\vec{q}_e \cdot \sum_{\zeta} \vec{x}^{(\zeta)}}$, while practically $e^{i\vec{q}_e \cdot \sum_{\zeta} \vec{x}^{(\zeta)}}$ is the electron boost operator.

Now we will assess the factor Z_{FI} , which is the sum of three probabilities as given in the Ref. [36],

$$\sum_F |Z_{FI}|^2 = |Z_{II}|^2 + |Z_{\text{exc}}|^2 + |Z_{\text{ion}}|^2. \quad (25)$$

Here $|Z_{II}|^2$ represents the probability that the electron is unaffected by the nuclear recoil (mention that this is the result in $\mathcal{O}(\frac{q_e^2}{(r)^2})$), whereas $|Z_{\text{exc}}|^2$ and $|Z_{\text{ion}}|^2$ denote the probabilities of electron excitation and ionization, respectively. The ionization factor $Z_{\text{ion}}(q_e)$ involve

$$Z_{\text{ion}}(q_e) = \langle F | e^{i\frac{m_e}{m_N} \vec{q} \cdot \sum_{\zeta} \vec{x}^{(\zeta)}} | I \rangle \sim \sum_{\zeta} \langle f | i\vec{q}_e \cdot \vec{x}^{(\zeta)} | i \rangle, \quad (26)$$

where m_e and m_N are the mass of the electron and nucleus, respectively. The last term of the above equation considers the leading order of the Taylor expansion of \vec{q}_e . We have made approximations by factoring the wave functions of the initial and final electron clouds, $|I\rangle$ and $|F\rangle$, so that only a single electron (with the position operator $\vec{x}^{(\zeta)}$, i.e. $\vec{x}^{(\zeta)}$ denotes the position of ζ^{th} electron in electron cloud.) involved in the transition between the single-electron states $|i\rangle$ and $|f\rangle$.

Furthermore, we will quickly write down the single-electron transition amplitude for the direct interaction of DM with the electron at coordinate $\vec{x}^{(\eta)}$,

$$\langle F | e^{i\vec{q} \cdot \sum_{\eta} \vec{x}^{(\eta)}} | I \rangle \sim \sum_{\eta} \langle f | i\vec{q} \cdot \vec{x}^{(\eta)} | i \rangle. \quad (27)$$

Comparing Eq. 26 and Eq. 27, we can see that the Migdal effect and DM-electron scattering are very similar in form, while the critical difference between them is the transfer momentum \vec{q}_e and \vec{q} . For the latter, the electrons directly obtain the momentum lost by the DM. The transfer momentum \vec{q}_e received by the electrons in the Migdal process is suppressed by a factor of $10^{-3}/A$ (here A is atomic mass number).

To calculate the electron ionization probability of the Migdal effect and electron scattering in isolated atoms, we rely on the work in the Ref. [19, 98, 100] to establish their precise relationship. From the dimensionless ionization form factor $|f_{\text{ion}}^{nl}(k_e, q)|^2$ defined in the

Ref. [19, 100], we can rewrite the Eq. 27 as

$$|Z_{\text{ion}}|^2 \equiv |f_{\text{ion}}^{nl}(k_e, q)|^2 = \frac{2k_e}{8\pi^3} \times \sum_{\substack{\text{occupied } l' m' \\ \text{states}}} \sum_{m'} |\langle k_e, l', m' | e^{i\vec{q} \cdot \vec{x}} | n, l \rangle|^2. \quad (28)$$

This represents the sum over final state angular variables l' , m' and degenerate, occupied initial states. The initial state wave function of bound electrons in isolated atoms is characterized by the principal quantum number n and the angular momentum quantum number l , and the final state is a continuous unbound electron state with momentum $k_e = \sqrt{2m_e E_e}$, which represents the quantum numbers are l' and m' . We adopt the ionization form factor $|f_{\text{ion}}^{nl}(k_e, q)|^2$ given in the work [85] to derive our results. However, the ionization form factor provided in their research does not adequately describe the ionization behavior of transfer momentum \vec{q} below 1 keV, hence we employ dipole approximation to extend it,

$$|f_{\text{ion}}^{nl}(k_e, q)|^2 = \left(\frac{q}{q_0}\right)^2 \times |f_{\text{ion}}^{nl}(k_e, q_0)|^2. \quad (29)$$

For the xenon atom, $q_0 \lesssim 1$ keV is usually chosen so that the above approximation holds.

According to the previous description and the Ref. [98], we utilize the parameter q_e to characterize the ionization probability of Migdal, it can be expressed as

$$\sum_{n,l} \frac{d}{d \ln E_e} dp_{q_e}^c(n, l \rightarrow E_e) = \frac{\pi}{2} |f_{\text{ion}}^{nl}(k_e, q_e)|^2. \quad (30)$$

Thus we can derive the ionization differential event rates induced by the Migdal effect in iDM-nucleus scattering,

$$\frac{dR}{dE_R dE_{\text{em}} dv} = \frac{dR_0}{dE_R dv} \times \frac{1}{2\pi} \sum_{n,l} \frac{d}{dE_e} dp_{q_e}^c(n, l \rightarrow E_e), \quad (31)$$

where

$$\frac{dR_0}{dE_R} = N_T \frac{\rho_\chi}{m_\chi} \int_{v > v_{\text{min}}} \frac{d\sigma}{dE_R} v f(v) d^3v. \quad (32)$$

This is decomposed into the standard elastic DM-nucleus scattering differential rate $\frac{dR_0}{dE_R}$ multiplied by the electron ionization probability, where $f(v)$ is the local velocity distribution function of the DM, ρ_χ is the local DM density (take $\rho_\chi \simeq 0.3 \text{ GeV/cm}^3$ in our calculations), N_T is the number density of target nuclei in the detector. The total electromagnetic energy E_{em} is defined as the sum of the outgoing unbound electron energy E_e and the binding

energy E_{nl} between the corresponding levels: $E_{\text{em}} = E_e + E_{nl}$. For Migdal scattering, the electron equivalent energy detected by the detector is given by

$$E_{\text{det}} = \mathcal{Q} E_R + E_{\text{em}} = \mathcal{Q} E_R + E_e + E_{nl}, \quad (33)$$

where \mathcal{Q} is the introduced quenching factor that depends on the nuclear recoil energy. The quenching factor of different target nucleus will also be different, and there have been a series of measurement results for xenon [101, 102]; here, we take a fixed $\mathcal{Q} = 0.15$ [36]. Finally we can obtain the detection energy spectrum,

$$\frac{dR}{dE_{\text{det}} dv} \simeq \int dE_R dE_{\text{em}} \frac{dR}{dE_R dE_{\text{em}} dv} \times \delta(E_{\text{det}} - \mathcal{Q} E_R - E_{\text{em}}). \quad (34)$$

B. Numerical Results and Discussions

To facilitate comparison with other results, we set the cross section of the DM-nucleon at transfer momentum $q = 0$ as

$$\bar{\sigma}_{\chi n}(q = 0) \equiv \frac{c_i^n{}^2 \mu_{\chi n}^2}{\pi}. \quad (35)$$

To compensate for the dimension of the coefficient $c_i^n (\text{Energy})^{-2}$, we have maintained the convention of multiplying by the square of electroweak interaction strength $m_v^{-2} \equiv (246.2 \text{ GeV})^{-2}$ in our calculations.

In Fig. 2, we calculated the nuclear recoil spectrum of inelastic dark matter-nucleus scattering to indicate to what extent the kinematics of the iDM-nucleus affects the event rate. For simplicity, we consider the dark matter with the mass splitting of δ and mass $m_\chi = 1 \text{ GeV}$ coupled to protons only. We can see two cases of inelastic scattering with a xenon atomic target when considering the individual spin-dependent operator \mathbf{O}_4 . the left panel is endothermic scattering, and the right panel is exothermic scattering. We scale the strength of the SD interaction at $c_i^p = 10^4$ to correspond to the reference cross section $\bar{\sigma}_{\chi p} \sim 10^{-30} \text{ cm}^2$ for SD interaction at $m_\chi = 1 \text{ GeV}$, and the value of nuclear recoil energy $E_R^{\text{max}}(E_R^{\text{min}})$ corresponds to $\theta = \pi$ ($\theta = 0$) in Eq. 12. For endothermic scattering, based on Eq. 8, it can be seen that with δ increasing, E_R^{max} decreases and E_R^{min} increases, and the peak nuclear recoil rate is reduced accordingly. This indicates that kinematically elastic scattering is more favourable than endothermic scattering, and this becomes more pronounced as δ becomes larger. For $m_\chi = 1 \text{ GeV}$, the maximum available initial-system kinetic energy is

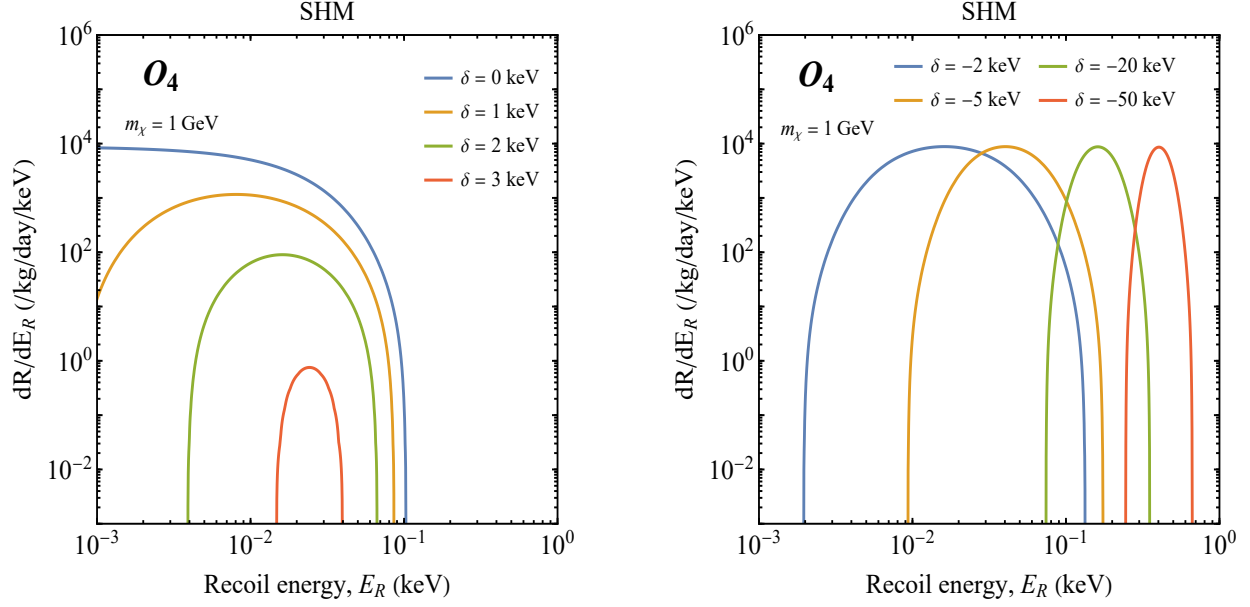


FIG. 2. The nuclear recoil spectrum is derived from the inelastic dark matter scattered with xenon atoms in the Standard Halo Model through spin-dependent interaction. Assuming $m_\chi = 1$ GeV, we show the endothermic scattering of the iDM-nucleus in the left panel, with different coloured solid lines depicting different δ , where $\delta = 0$ (blue), 1 (orange), 2 (green), and 3 keV (red). The right panel shows the process of exothermic scattering, where $\delta = -2$ (blue), -5 (orange), -20 (green), and -50 keV (red).

about 3.2 keV, while δ is larger than this value, the rate cannot be generated, as shown in the left panel of the figure. On the other hand, in exothermic scattering with $\delta < 0$, due to the fixed maximum incoming velocity of the DM, the peak of the recoil spectrum does not drop, both E_R^{min} and E_R^{max} increase with increasing $|\delta|$. This illustrates that for larger $|\delta|$, the scattering is more (less) kinematically favored for sufficiently small (large) energies.

In xenon-based detectors, ionized electrons produced by Migdal can be detected, so we depict the differential event rates as a function of the detected energy (in units of keV electron equivalent, keV_{ee}) by inducing the SD (\mathbf{O}_4) interaction with xenon in Fig. 3 (consider the incoming DM particle $m_\chi = 1$ GeV). Note that to facilitate comparisons, we will scale the coupling strength to expect nuclear recoils up to 10^4 . To illustrate their characteristics, we use the solid black line represents the spectrum for nuclear recoil, the colored solid lines represent the Migdal scattering rates induced by different electron energy levels determined by n , and the dashed line gives the effect caused by different mass splitting δ on the same

electron shell.

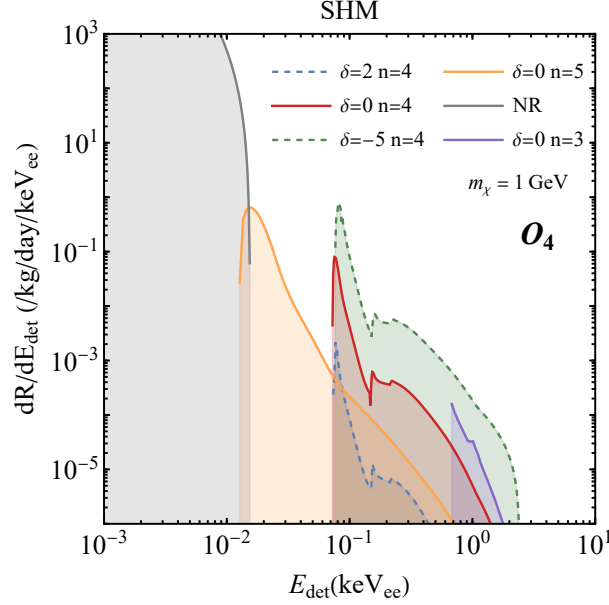


FIG. 3. The rate of Migdal events induced by a mass $m_\chi = 1$ GeV dark matter particle scattering with the nucleus through the spin-dependent interaction for the xenon target in SHM. Coloured solid lines depict the contributions of various atomic energy levels represented by n . For $n = 4$, we depict the endothermic (exothermic) scattering in Migdal with a blue (green) dashed line, where $\delta = 2$ keV ($\delta = -5$ keV). The black solid line depicts the elastic nuclear recoil.

Firstly, for the xenon atom, it is obvious that the Migdal rate is different for the energy level n occupied by each electron: larger n is more sensitive to lower E_{det} , and the peak of the recoil spectrum is also higher. This is because the more outer electrons are more easily excited/ionised and therefore have more sensitivity to lower threshold detection energies. Secondly, comparing the Migdal rates for the same electron energy level, we can see that for endothermic scattering, there is an overall decrease in the recoil spectrum and the opposite for exothermic scattering, but for both, there is no abrupt change in the shape of the spectrum. The peak of the Migdal rate is determined by the minimum energy (i.e. the energy released by the de-excitation of the higher shell electrons to fill the orbits corresponding to the Migdal electron transitions), and occurs exactly at the minimum energy for any shell. Consequently, this quantity is determined by n and is largely independent of the dark matter parameter.

Although we have included the nuclear recoil spectrum in Fig. 3, it is important to note

that this is only to compare the Migdal spectrum ($E_{\text{det}} = \mathcal{Q}E_R$ for elastic nuclear recoil). For $m_\chi = 1$ GeV dark matter, the Migdal rate becomes the dominant rate with E_{det} above $100 \text{ keV}_{\text{ee}}$, thus implying that at lower detector thresholds the Migdal effect would be more beneficial in providing an effective window for exploring low-mass dark matter.

In direct detection experiments, the number of the events are closely related to the scattering cross section of dark matter. Therefore, after calculating the rate, we will use the results of the Migdal effect and scattering after endothermic (exothermic) to give new limits on the spin EFT operator \mathbf{O}_4 for low-mass dark matter. We have kept only the ionization factor for $n = 4, 5$ in our calculations because the rate at $n = 3$ is extremely small as can be seen from Fig. 3, so we have ignored it. We give the corresponding bounds based on the data provided by the XENON1T experiment. This experiment accepts two main signals: primary scintillation light (S1), which is generated by nuclear recoil and can be detected directly, and delayed proportional scintillation (S2), which is measured as a proportional signal when a drifting electron is extracted into the gas phase. The signals S1 and S2 allow for the discrimination of nuclear/electronic recoil, and electron recoils produces events with larger S2/S1 than nuclear recoils.

Here, we have used here the single ionisation channel S2 data set from XENON1T [2] for the analysis. In the S2-only case, although this reduces the background discrimination and lifetime, it allows the lower threshold to enter the analysis. This case does not distinguish between nuclear and electronic recoil, thus establishing cross section bounds for different cases of low-mass WIMPs. Based on the experimental thresholds for XENON1T, it is reasonable to integrate the rate of events in the range $E_{\text{det}} = 0.186 - 3.8 \text{ keV}_{\text{ee}}$ in order to implement a single bin analysis (no signal is seen below 0.186 keV) and to consider taking into account the energy dependent efficiency. At an exposure of 22 tonne-day, the expected number of events from the background was $n_{\text{exp}} = 23.4$, while the total number of observed events was $n_{\text{obs}} = 61$. From these data, using the profile likelihood ratio [103] gives an upper limit of 48.9 for the number of events expected for dark matter at 90% C.L. For the latest liquid xenon (LXe) detector, LUX-ZEPLIN (LZ), which has a higher sensitivity to nuclear recoil energies at the $\mathcal{O}(\text{keV})$ level [104, 105]. We used the energy dependent efficiency of XENON1T to integrate over the range $E_{\text{det}} = 0.5 - 4 \text{ keV}_{\text{ee}}$, assuming a 5.6 tonne material exposure for 1000 days, an expected event rate of $2.5 \times 10^{-5} (\text{/kg/day/keV})$ from ^{220}Rn for the background, and an uncertainty of 15% for the background [105], and finally obtain an

upper limit on the expected number of events of 79.6.

In Fig. 4, using S2-only data from XENON1T, we compare the effects of three velocity distribution models on the iDM-nucleus Migdal scattering cross section in the spin-dependent interactions. We have marked the SHM with a solid line, the Empirical model with dashed line and the Tsallis model with dash-dotted line. We can observe that, as an overall trend, the bounds of the Tsallis model is weaker than that of the SHM and Empirical model for all three interactions: endothermic ($\delta = 5$ keV), elastic ($\delta = 0$ keV), and exothermic ($\delta = -5$ keV), with this difference more apparent in the elastic and endothermic. There is even an order of magnitude difference between them. The empirical model is only slightly stronger than the SHM limit above the DM mass of 0.1 GeV (for $\delta = 0$ keV). These situation can be traced back to Fig. 1, where the $\eta(v_{\min})$ of the Tsallis model falls more rapidly at greater than 300 km/s. Therefore, for larger v_{\min} (see Eq. 13), the smaller the value of $\eta(v_{\min})$, the weaker the associated generating bounds. Returning to Eq. 13, exothermic scattering makes it easier for DM with masses in the $10^{-3} \sim 1$ GeV region to fall in the low-velocity region. The three models almost overlap for DM masses below 1 GeV, indicating that lower masses of DM retain more flexibility in the choice of VDFs.

In Fig. 5, for the spin-dependent operator \mathbf{O}_4 , after accounting for elastic, exothermic and endothermic interactions, we show the constraints on the cross section for XENON1T and LZ experiments coupled with protons and neutrons alone at 90% C.L., respectively. Even for different couplings, the various bound shapes are quite similar, and the elastic scattering provides a good analogy: the Migdal effect shows more limits than the elastic nuclear recoil around $m_\chi \simeq 3$ GeV, below which the bounds all originate from the Migdal effect and yield more bounds for the lower masses of dark matter. In fact, the crossover point between the Migdal and nuclear recoil boundary is determined by the threshold reached by the detector. Under the spin-dependent operator \mathbf{O}_4 , the degree of constraint on the proton and neutron cross sections differs, with the cross section of the proton being weaker than that of the neutron since the xenon isotope, which has an even number of protons ($Z = 54$), the spin expectation value of the proton is smaller after the intrinsic spin magnetic moments offset each other.

On the one side, we notice that the bounds of endothermic scattering is very closer to that of elastic scattering. According to Eq. 22, as the mass loss δ increases in endothermic scattering, the approximate maximum available energy projected to the Migdal electron

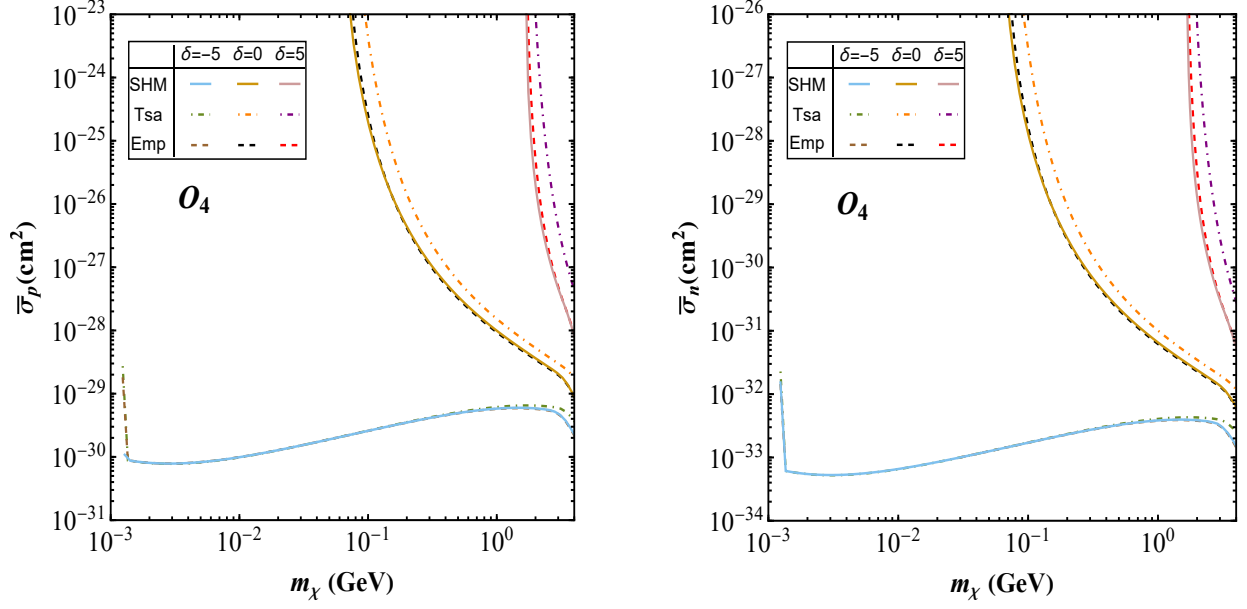


FIG. 4. Constraints (90% C.L.) from three velocity distribution functions on the iDM-nucleus Migdal effect of the spin-dependent interaction. We depict the bounds of Tsallis, Empirical and Standard Halo Model with dash-dotted, dashed and solid lines, respectively. The coloured lines depict the impacts of different DM mass splitting on the bounds at each velocity distribution, where $\delta = -5, 0, 5$ keV respectively. The left panel represents the interaction of DM with proton-only coupling, and the right panel represents the interaction with neutron-only coupling.

decreases, so the bounds loses sensitivity to low-mass dark matter more rapidly. On the other side, Migdal electrons in exothermic scattering can acquire more energy so that they still have above-threshold sensitivity at lower DM masses. Essentially, Migdal electrons are easily excited above the threshold because for DM with masses below GeV, $\frac{1}{2}m_\chi v^2 \sim \mathcal{O}(\text{keV})$, then $\delta \sim \mathcal{O}(\text{keV})$, there is a significant enhancement effect. For DM masses below $m_\chi \sim 10$ MeV, the limiting boundary of LZ is clearly weaker than that of XENON1T, due to the fact that we predict a higher threshold for LZ ($E_{\text{det}} \geq 0.5 \text{ keV}_{\text{ee}}$) than for the S2-only analysis of XENON1T.

In addition, we set a cut-off value for the E_R in Migdal process, as mentioned in Ref. [106]. In calculating the ionisation function, for the impulse approximation to hold, it is necessary to ensure that the collision time $t_{\text{collision}} \sim 1/E_R$ is less than the time $t_{\text{traverse}} \sim 1/\omega_{ph}$ (ω_{ph} is the phonon frequency) for the atom to traverse its potential field. For sufficiently small DM masses, there will be recoil energy falling below this cut-off value and the Migdal rate will

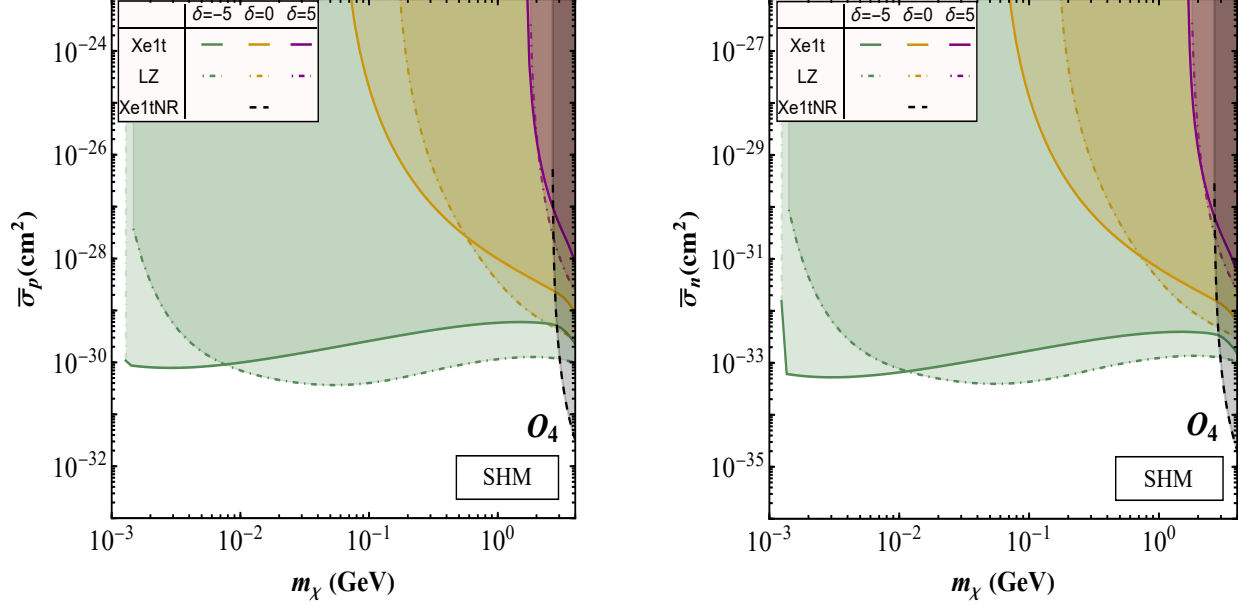


FIG. 5. The 90% C.L. limits on the iDM-nucleus scattering cross section of spin-dependent interaction from XENON1T on nuclear recoils (dashed), XENON1T with the Migdal effect (solid) and the projected LZ sensitivity with the Migdal effect (dash-dotted). The coloured lines depict the different scattering processes, where $\delta = 5$ keV for endothermic (purple), $\delta = -5$ keV for exothermic (green), and $\delta = 0$ keV for elastic scattering (orange). We plot the scattering cross sections of the iDM coupling with protons and neutrons in the left and right panels, respectively.

fail, so this value has a relatively large impact on the detector threshold as well as on the low dark matter masses. Referring to the method in Ref. [24], use the time $t \sim \mathcal{O}(10^{-12})s$ required for a xenon atom to traverse the average interatomic distance at 170k at the speed of sound as the cut-off time. We conservatively to set $E_{R\text{cut}} \geq 50$ meV. Thus, we can place a limit on the mass of dark matter: elastic scattering corresponds to 0.02 GeV, while exothermic (endothermic) scattering relies on the mass splitting $\delta = -5$ keV (5 keV), which is 0.001 GeV (0.36 GeV).

IV. INELASTIC DARK MATTER-ELECTRON SCATTERING

This section will investigate inelastic dark matter-electron scattering [30, 107–109] in a non-relativistic effective field theory. Mainly derive the formula we need for calculation.

A. Calculations

From a kinematic point of view, inelastic dark matter-electron scattering is essentially the same as the previously described inelastic dark matter-nucleus scattering, but with a different target, $\chi(\vec{p}) + e(\vec{k}) \rightarrow \chi'(\vec{p}') + e(\vec{k}')$. In contrast to the dynamics of the Migdal effect, the electron spectrum of Migdal is assessed using the effective transfer momentum $\vec{q}_e \equiv \frac{m_e}{m_N} \vec{q}$, which is the most significant difference from electron scattering. For the energy conservation of the iDM-electron scattering process, it is simple to rewrite Eq. 21 as $E_{\text{em}} + \delta = \vec{q} \cdot \vec{v} - \frac{q^2}{2\mu_{\chi e}}$, where $\mu_N \rightarrow \mu_{\chi e}$ ($\mu_{\chi e}$ is the reduced mass of the DM and electron). Furthermore, when the maximum incoming velocity v_{max} of the DM is fixed, we can determine the range of allowed momentum transfers. The minimum and maximum momentum transfer are

$$q_{\text{min}} = \text{sign}(E_{\text{em}} + \delta) m_{\chi} v_{\text{max}} \left(1 - \sqrt{1 - \frac{2(E_{\text{em}} + \delta)}{m_{\chi} v_{\text{max}}^2}} \right) \quad (36)$$

$$q_{\text{max}} = m_{\chi} v_{\text{max}} \left(1 + \sqrt{1 - \frac{2(E_{\text{em}} + \delta)}{m_{\chi} v_{\text{max}}^2}} \right)$$

In the limit $\delta \rightarrow 0$ Eq. 36 reduces to elastic scattering.

Similarly to nuclear, we also introduce an effective field theory for iDM-electron scattering according to the work of Catena et al [110]. In this formalism, the active degrees of freedom will be DM particles and electrons. The symmetry governing non-relativistic DM-electron scattering is replaced by Galilean invariance instead of Lorentz invariance under relativistic boosted. Thus, the invariant amplitude of DM-electron scattering can still be represented by a series of operators consisting of Galilean invariants.

In this EFT, there are also four three-momentum Galilean invariants: \vec{q} , \vec{S}_e , \vec{S}_{χ} , $\vec{v}_{\text{inel}}^{\perp}$. Here corresponding to the inelastic case, $\vec{v}_{\text{inel}}^{\perp}$ is defined as

$$\vec{v}_{\text{inel}}^{\perp} \equiv \vec{v} + \frac{\vec{q}}{2\mu_{\chi e}} + \frac{\Delta}{|q|^2} \vec{q} \quad (37)$$

where $\mu_{\chi e}$ is the reduced mass of the DM and electron. Since the conservation of energy in the iDM-electron scattering process, $\vec{v}_{\text{inel}}^{\perp} \cdot \vec{q} = 0$. Compared with the definition of Eq. 14, we can see that the process of inelastic scattering of electrons only modifies $\mu_N \rightarrow \mu_{\chi e}$. Also, this modification is only reflected in the DM particle response function \mathcal{R}_i^{nl} . For the operator $\mathbf{O}_4 = \vec{S}_e \cdot \vec{S}_{\chi}$, it is not subject to $\vec{v}_{\text{inel}}^{\perp}$, so we can still refer to the results of the elasticity calculation in Ref.[110].

It is worth noting that in this EFT, the invariant scattering amplitude $\mathcal{M}(\vec{q}, \vec{v}_{\text{inel}}^\perp)$ of the DM-electron does not depend explicitly on the characteristics of the specific mediator particle. However, this formalism is still applicable when the mediator particle mass is much larger than the transfer momentum: $m_{\text{med}}^2 \gg q^2$ (contact interaction), or much smaller than the transfer momentum: $m_{\text{med}}^2 \ll q^2$ (long-range interaction) [111]. To summarise these, the free amplitudes of non-relativistic iDM-electron scattering express as

$$\mathcal{M}(\vec{q}, \vec{v}_{\text{inel}}^\perp) = \sum_i \left(c_i^s + c_i^l \frac{q_{\text{ref}}^2}{|q|^2} \right) \langle \mathbf{O}_i \rangle, \quad (38)$$

where the reference momentum $q_{\text{ref}} \equiv \alpha m_e$, $\alpha = 1/137$, and the coefficient c_i^s (c_i^l) represents the contact (long-range) interaction of the DM particle with the electron.

To obtain the total event rate we are interested in, first, the total transition rate of electrons induced by DM for the initial state of electron $|e_1\rangle \rightarrow$ final state $|e_2\rangle$ is

$$\mathbb{R}_{1 \rightarrow 2} = \frac{n_\chi}{16m_\chi^2 m_e^2} \int \frac{d^3 q}{(2\pi)^3} \int d^3 v v f(v) (2\pi) \delta(E_f - E_i) \overline{|\mathcal{M}_{1 \rightarrow 2}|^2}, \quad (39)$$

where $n_\chi = \rho_\chi/m_\chi$ is the local DM number density, E_f (E_i) is the final (initial) state energy of the system, and the δ function ensures the conservation of energy for this process. $\overline{|\mathcal{M}_{1 \rightarrow 2}|^2}$ was defined as the squared electron transition amplitude [110],

$$\overline{|\mathcal{M}_{1 \rightarrow 2}|^2} = \left| \int \frac{d^3 k}{(2\pi)^3} \psi_2^*(\vec{k} + \vec{q}) \mathcal{M}(\vec{q}, \vec{v}_{\text{inel}}^\perp) \psi_1(\vec{k}) \right|^2. \quad (40)$$

Here ψ_1 and ψ_2 represent the electron initial and final state wave functions, respectively, and this equation has been averaged (summed) over the initial (final) spin states. Then, we can write down the iDM-electron scattering differential event rates that include the full atomic orbitals

$$\begin{aligned} \frac{dR}{d \ln E_e} &= \sum_{m=-l}^l \sum_{l'=0}^\infty \sum_{m'=-l'}^{l'} \frac{V k'^3}{(2\pi)^3} \mathbb{R}_{1 \rightarrow 2} \\ &= \frac{n_\chi}{128\pi m_\chi^2 m_e^2} \int dq q \int d^3 v v f(v) \Theta(v - v_{\text{min}}) \overline{|\mathcal{M}_{\text{ion}}^{nl}|^2}, \end{aligned} \quad (41)$$

where $V = (2\pi)^3 \delta^3(0)$ is the normalized phase space factor [112], Θ is a step function to ensure that the incoming speed of the DM reaches the energy required to cause the electron

recoil. And $|\overline{\mathcal{M}_{\text{ion}}^{nl}}|^2$ is the so-called electron ionisation amplitude squared, defined as

$$\begin{aligned} |\overline{\mathcal{M}_{\text{ion}}^{nl}}|^2 &\equiv V \frac{4k'^3}{(2\pi)^3} \sum_{m=-l}^l \sum_{l'=0}^{\infty} \sum_{m'=-l'}^{l'} |\overline{\mathcal{M}_{1 \rightarrow 2}}|^2 \\ &= \sum_{i=1}^4 \mathcal{R}_i^{nl} \left(\vec{v}_{\text{inel}}^{\perp}, \frac{\vec{q}}{m_e} \right) \mathcal{W}_i^{nl}(k', \vec{q}), \end{aligned} \quad (42)$$

where getting from the first expression to the second is actually a Taylor expansion of $\mathcal{M}(\vec{q}, \vec{v}_{\text{inel}}^{\perp})$ at $\vec{k} = 0$, which is then expressed as a product of the DM particle response function \mathcal{R}_i^{nl} and the associated atomic response function \mathcal{W}_i^{nl} . This approach allows for a more intuitive examination of the DM-electron scattering process.

In fact, there are four atomic response functions that can be derived from Ref.[110]. In our work, only \mathcal{W}_1^{nl} was applied

$$\mathcal{W}_1^{nl}(k', \vec{q}) \equiv V \frac{4k'^3}{(2\pi)^3} \sum_{m=-l}^l \sum_{l'=0}^{\infty} \sum_{m'=-l'}^{l'} |f_{1 \rightarrow 2}(q)|^2. \quad (43)$$

For \mathcal{W}_1^{nl} , it is actually the ionization factor commonly used in various light dark matter detection literatures. The $f_{1 \rightarrow 2}(\vec{q})$ in the above expression is called the scalar form factor

$$f_{1 \rightarrow 2}(\vec{q}) = \int \frac{d^3k}{(2\pi)^3} \psi_2^*(\vec{k} + \vec{q}) \psi_1(\vec{k}). \quad (44)$$

Corresponding to our calculation, the DM response function is $\mathcal{R}_1^{nl} \equiv \frac{j_X(j_X+1)}{4} c_4^2$.

B. Numerical Results and Discussions

The non-relativistic effective theory of iDM-electron interactions described in the previous subsection culminates in a general expression for the electron ionization energy spectrum of isolated atoms constructed from Eq. 41. This almost model-independent framework and a general expression for the scattering amplitude consisting of a series of effective operators in Eq. 42 allow us to make predictions for direct searches for sub-GeV DM particles. For comparison purposes, we keep to the formalism in Ref. [110] and also give a reference cross-section for the electron,

$$\bar{\sigma}_e \equiv \frac{\mu_{\chi e}^2 c_i^2}{16\pi m_{\chi}^2 m_e^2}. \quad (45)$$

This definition differs from the reference cross section of the nucleus, where c_i does not require additional compensation for the dimensions. The contact and long-rang interaction

can then be identified using individual EFT operators and the connection between the EFT coefficients in Eq. 38. In particular, we take into account the effects of inelasticity to compare the electron ionization events induced within the detector threshold.

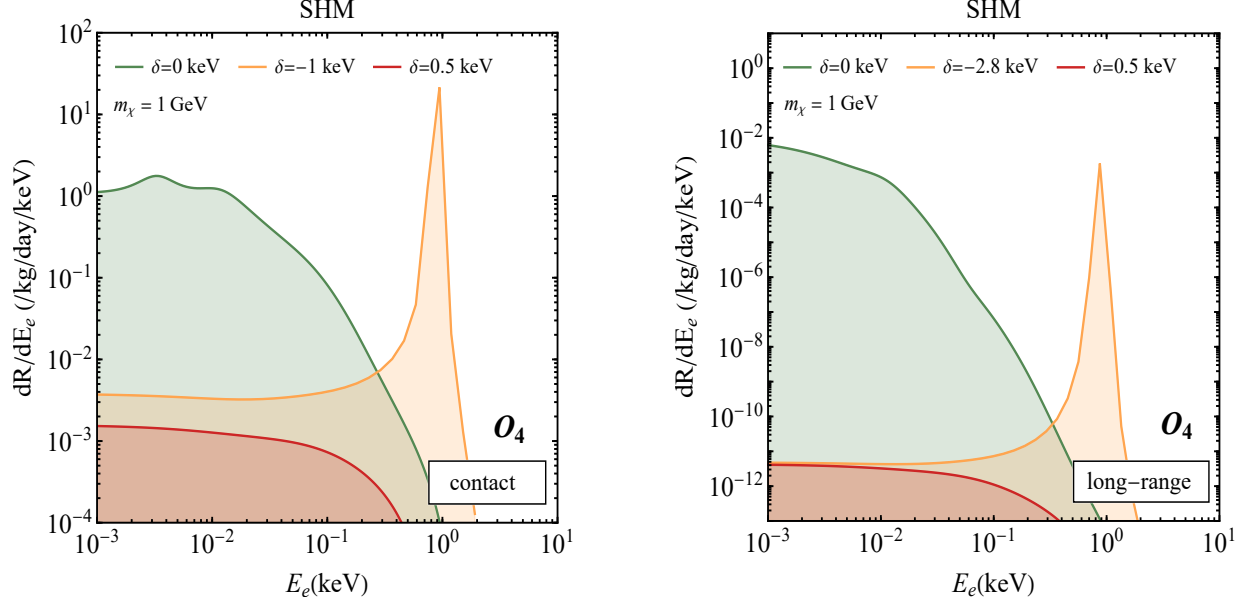


FIG. 6. The differential event rates for inelastic dark matter of mass $m_\chi = 1$ GeV through contact (left) and long-range (right) interactions with electron scattering on the spin-dependent operator \mathbf{O}_4 , respectively. The endothermic (red), elastic (green), and exothermic (orange) scattering are depicted with solid lines of various colors corresponding to $\delta = 0.5, 0, -1$ keV, respectively.

In Fig. 6, we use $\delta = 0, 0.5, -1$ keV as fiducial parameters to show the differential event rates of elastic, endothermic and exothermic scattering of DM with electrons when applying an individual spin operator \mathbf{O}_4 at contact and long-range interactions, respectively. Here we set the coefficient $c_4 = 10^{-6}$ for \mathbf{O}_4 , corresponding to the spin cross section $\bar{\sigma}_e^{\text{SD}} \sim \mathcal{O}(10^{-40}) \text{ cm}^2$, assume that DM particles obey the velocity distribution of SHM and the mass of incident DM particle $m_\chi = 1$ GeV. In recent studies [113], it has been pointed out that a scaling factor of $\xi = \mathcal{W}_1^{\text{nl}(\text{SD})} / \mathcal{W}_1^{\text{nl}(\text{SI})}$ for the first electronic response functions of SI and SD, with $\xi = 3$ for the commonly applied model. This scaling factor $\xi = 3$ is valid for xenon when the electron energy $E_e \lesssim 0.2$ keV for the case of $m_\chi = 1$ GeV. Moreover, the scaling deviation starts to grow as E_e increases, but in our work, we keep setting $\xi = 3$ constant. Furthermore, in iDM-electron scattering, the ionization event rate is severely suppressed for endothermic compared to elastic scattering and is more significant

for long-range interactions. This is because for elastic and endothermic scattering they produce typical recoil energies $\mu_{\chi e} v_{\max}^2 \sim \mathcal{O}(\text{eV})$. Endothermic scattering does not have better sensitivity than elastic for usual xenon-type detectors. In exothermic scattering, the events spectrum in the figure shows a sharp peak around $E_e \simeq |\delta|$, followed by a sharp drop after $E_e > |\delta|$. This relationship can be understood from Eq. 36: when $E_{\text{em}} = |\delta|$, the lower limit of transfer momentum $q_{\min} = 0$ and the upper limit $q_{\max} = 2m_\chi v_{\max}$, at which point the integration of the ionisation function over \vec{q} leads to a strong enhancement of the scattering rate. Note that this enhancement is a feature of exothermic scattering, so that the differential rate is largely independent of the mass of the DM in the mass range we are concerned with.

Finally, similar previous analyses are used to give electron scattering cross sections that match the XENON1T S2-only data and to predict limits for future LZ experiment (90%C.L.). The three different velocity distribution models are still taken into account, and we keep the exothermic (endothermic) scattering parameter of $\delta = -1 \text{ keV}$ (0.5 keV) to demonstrate the inelastic effect on an individual effective spin-dependent operator in the contact/long-range interaction, as shown in Fig. 7.

The iDM-electron scattering bounds resembles Migdal’s behaviour in Fig. 5. Exothermic scattering retains more sensitivity to low-mass dark matter, while endothermic scattering preserves the opposite property. This is where we discussed earlier that there is no difference in kinematics between Migdal and electron scattering, with the transfer momentum \vec{q} being the crucial difference between them (reflected in the different regions of the ionization function). As mentioned previously, the effects of the velocity distribution remain slight, and only the Tsallis model differs from the other two models at higher velocity tails. Interestingly, we note that the bounds of exothermic scattering seem to extend to lower mass regions. Because according to Eq. 36, there is always $q_{\min, \max} \neq 0$ when $E_{\text{em}} < |\delta|$. Thus if no other physical constraints exist, the section will naturally cut off at $m_\chi = |\delta|$. For long-range interactions, the cross section is constrained by $\sim 1/q^4$ and the bounds is instead strengthened when the transfer momentum $q < 1 \text{ keV}$. Although the prediction of exothermic scattering for LZ is superior to that of XENON1T in the mass range $m_\chi \sim (1 \text{ MeV} - 1 \text{ GeV})$, we have adopted a more optimistic analysis of LZ’s S2-only, $n_{\text{obs}} = n_{\text{exp}}$, which would result in a lower threshold for LZ. For this analysis of LZ, the achievable thresholds, background, and exposure are unknown.

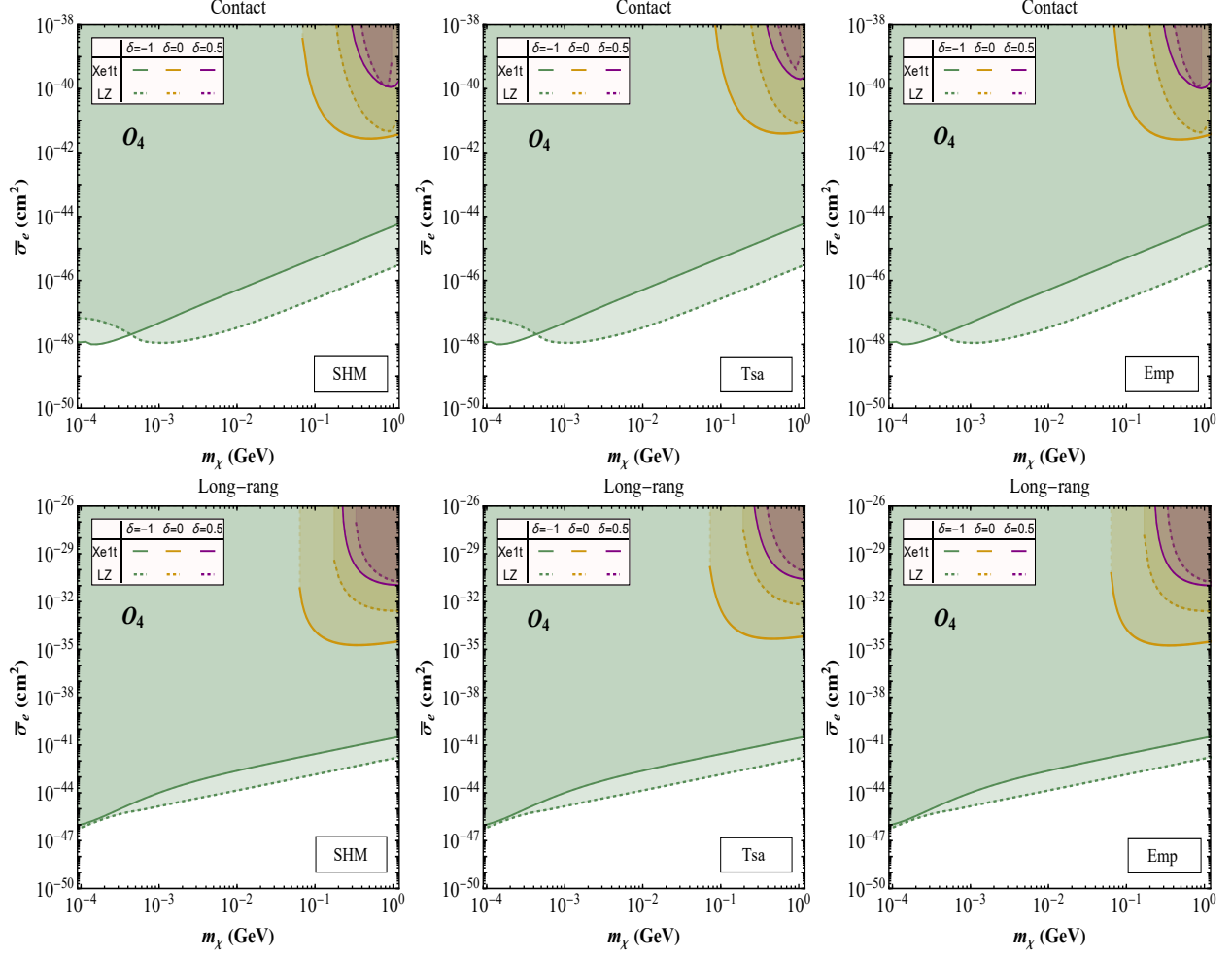


FIG. 7. The 90% C.L. constraints on iDM-electron cross section $\bar{\sigma}_e$ versus DM mass m_χ from the spin-dependent contact (top) and long-range (bottom) interaction for different mass splitting δ and three velocity distribution models. We used the S2-only data from XENON1T for analysis and projected the bounds of the LZ experiment. These processes are exothermic with $\delta = -1$ keV (green), elastic with $\delta = 0$ keV (orange), endothermic with $\delta = 0.5$ keV (purple) scattering, and include Standard Halo Model (left panel), Tsallis Mode (middle panel), Empirical Model (right panel).

V. CONCLUSION

Although experimental work in direct dark matter detection has yielded fantastic results for exploring the DM parameter space, dark matter remains invisible in the heavy mass region. The future detection of sub-GeV dark matter remains a significant challenge. For

sub-GeV dark matter, the electron spectrum induced by the Migdal effect and DM-electron scattering provides a detectable window for direct detection experiments near low thresholds. However, the features of inelastic dark matter and the velocity distribution functions from different dark matter halos can have a critical impact on this electron spectrum. In this paper, we consider inelastic dark matter characterised by mass splitting δ . We use a concise non-relativistic effective field theory to study the Migdal effect and electron scattering induced by inelastic dark matter through spin-dependent interaction. Finally, the inelastic dark matter-nucleus Migdal/electron scattering cross sections are derived using data from XENON1T by importing the Tsallis, an Empirical and Standard Halo model of the velocity distribution function.

Comparing the three velocity distribution models, we find that the scattering cross section becomes more sensitive to DM velocities falling in the large v_{\min} region. However, regardless of the type of scattering, the Tsallis model has weaker constraints on the cross section than the other two models, although this is less pronounced in exothermic scattering. In elastic, endothermic scattering, the Tsallis model can be even an order of magnitude different than the other two models. In the case of DM masses above 0.1 GeV ($\delta = 0$), the empirical model is only stronger than the SHM. For exothermic scattering, the cross sections of the three models almost overlap for DM lighter than 1 GeV. This situation also allows more resilience in the choice of VDFs for low-mass dark matter. On the other hand, in assessing the Migdal effect for iDM-nucleus spin-dependent interactions, we considered couplings to proton or neutron only since isospin violation. In the exothermic scattering of Migdal, corresponds to the fiducial value $\delta = -5$ keV in our work, the bounds for neutron couplings is always stronger than for proton, up to $\sim \mathcal{O}(10^{-33}) \text{ cm}^2$ and $\sim \mathcal{O}(10^{-30}) \text{ cm}^2$ for proton. The endothermic scattering of Migdal ($\delta = 5$ keV) provides sensitivity near only a few GeV compared to the elastic nuclear recoil, but there is still no advantage for Migdal scattering at $\delta = 0$. In iDM-electron scattering, the cross section for long-range interactions is depressed by $\sim (1/q^2)^2$ and thus is weaker than the limit for contact interactions. In exothermic scattering, however, the bounds for long-range interactions is enhanced in the region where the DM mass is below ~ 1 MeV due to the $q < 1$ keV. These indicate that in the Migdal and electron scattering induced by iDM, exothermic scattering can produce sensitivity even for dark matter below 1 MeV. Although we consider xenon atoms, this result perhaps gives us a good insight into other targets and the search for dark matter at lower masses. In addition,

the LZ also has a higher sensitivity to exothermic scattering compared to the XENON1T, which may allow us to expect surprising results in future LZ experiment.

VI. ACKNOWLEDGEMENTS

We appreciate James Blackman Dent for the code and helpful discussions on inelastic dark matter scattering in the EFT context. This work is supported by the National Natural Science Foundation of China (NNSFC) under grants No. 12275134, by Natural Science Foundation of Shandong Province under the grants ZR2018QA007.

-
- [1] E. Aprile *et al.* (XENON), [Phys. Rev. Lett. **121**, 111302 \(2018\)](#), [arXiv:1805.12562 \[astro-ph.CO\]](#).
 - [2] E. Aprile *et al.* (XENON), [Phys. Rev. Lett. **123**, 251801 \(2019\)](#), [arXiv:1907.11485 \[hep-ex\]](#).
 - [3] D. Akimov *et al.* (COHERENT), [Science **357**, 1123 \(2017\)](#), [arXiv:1708.01294 \[nucl-ex\]](#).
 - [4] E. Aprile *et al.* (XENON), [Phys. Rev. D **102**, 072004 \(2020\)](#), [arXiv:2006.09721 \[hep-ex\]](#).
 - [5] R. Agnese *et al.* (SuperCDMS), [Phys. Rev. Lett. **121**, 051301 \(2018\)](#), [Erratum: [Phys.Rev.Lett. **122**, 069901 \(2019\)](#)], [arXiv:1804.10697 \[hep-ex\]](#).
 - [6] M. Crisler, R. Essig, J. Estrada, G. Fernandez, J. Tiffenberg, M. Sofo haro, T. Volansky, and T.-T. Yu (SENSEI), [Phys. Rev. Lett. **121**, 061803 \(2018\)](#), [arXiv:1804.00088 \[hep-ex\]](#).
 - [7] X. Ren *et al.* (PandaX-II), [Phys. Rev. Lett. **121**, 021304 \(2018\)](#), [arXiv:1802.06912 \[hep-ph\]](#).
 - [8] P. Agnes *et al.* (DarkSide), [Phys. Rev. Lett. **121**, 081307 \(2018\)](#), [arXiv:1802.06994 \[astro-ph.HE\]](#).
 - [9] D. S. Akerib *et al.* (LUX), [Phys. Rev. Lett. **122**, 131301 \(2019\)](#), [arXiv:1811.11241 \[astro-ph.CO\]](#).
 - [10] L. Barak *et al.* (SENSEI), [Phys. Rev. Lett. **125**, 171802 \(2020\)](#), [arXiv:2004.11378 \[astro-ph.CO\]](#).
 - [11] Q. Arnaud *et al.* (EDELWEISS), [Phys. Rev. Lett. **125**, 141301 \(2020\)](#), [arXiv:2003.01046 \[astro-ph.GA\]](#).
 - [12] E. Armengaud *et al.* (EDELWEISS), [Phys. Rev. D **99**, 082003 \(2019\)](#), [arXiv:1901.03588 \[astro-ph.GA\]](#).

- [13] D. S. Akerib *et al.* (LUX), [Phys. Rev. Lett. **118**, 021303 \(2017\)](#), [arXiv:1608.07648 \[astro-ph.CO\]](#).
- [14] D. Zhang *et al.* (PandaX), [Phys. Rev. Lett. **129**, 161804 \(2022\)](#), [arXiv:2206.02339 \[hep-ex\]](#).
- [15] W. Wang, L. Wu, W.-N. Yang, and B. Zhu, (2021), [arXiv:2111.04000 \[hep-ph\]](#).
- [16] L. Su, W. Wang, L. Wu, J. M. Yang, and B. Zhu, [Phys. Rev. D **102**, 115028 \(2020\)](#), [arXiv:2006.11837 \[hep-ph\]](#).
- [17] W. Wang, L. Wu, J. M. Yang, H. Zhou, and B. Zhu, [JHEP **12**, 072 \(2020\)](#), [Erratum: JHEP 02, 052 (2021)], [arXiv:1912.09904 \[hep-ph\]](#).
- [18] A. Aguilar-Arevalo *et al.* (DAMIC), [Phys. Rev. Lett. **123**, 181802 \(2019\)](#), [arXiv:1907.12628 \[astro-ph.CO\]](#).
- [19] R. Essig, J. Mardon, and T. Volansky, [Phys. Rev. D **85**, 076007 \(2012\)](#), [arXiv:1108.5383 \[hep-ph\]](#).
- [20] M. J. Dolan, F. Kahlhoefer, and C. McCabe, [Phys. Rev. Lett. **121**, 101801 \(2018\)](#), [arXiv:1711.09906 \[hep-ph\]](#).
- [21] J. D. Vergados and H. Ejiri, [Phys. Lett. B **606**, 313 \(2005\)](#), [arXiv:hep-ph/0401151](#).
- [22] G. Grilli di Cortona, A. Messina, and S. Piacentini, [JHEP **11**, 034 \(2020\)](#), [arXiv:2006.02453 \[hep-ph\]](#).
- [23] W. Wang, K.-Y. Wu, L. Wu, and B. Zhu, [Nucl. Phys. B **983**, 115907 \(2022\)](#), [arXiv:2112.06492 \[hep-ph\]](#).
- [24] N. F. Bell, J. B. Dent, B. Dutta, S. Ghosh, J. Kumar, and J. L. Newstead, [Phys. Rev. D **104**, 076013 \(2021\)](#), [arXiv:2103.05890 \[hep-ph\]](#).
- [25] N. F. Bell, J. B. Dent, J. L. Newstead, S. Sabharwal, and T. J. Weiler, [Phys. Rev. D **101**, 015012 \(2020\)](#), [arXiv:1905.00046 \[hep-ph\]](#).
- [26] V. V. Flambaum, L. Su, L. Wu, and B. Zhu, (2020), [arXiv:2012.09751 \[hep-ph\]](#).
- [27] G. Guo, Y.-L. S. Tsai, M.-R. Wu, and Q. Yuan, [Phys. Rev. D **102**, 103004 \(2020\)](#), [arXiv:2008.12137 \[astro-ph.HE\]](#).
- [28] Z. Y. Zhang *et al.* (CDEX), (2022), [arXiv:2206.04128 \[hep-ex\]](#).
- [29] H. An and D. Yang, [Phys. Lett. B **818**, 136408 \(2021\)](#), [arXiv:2006.15672 \[hep-ph\]](#).
- [30] W. Chao, Y. Gao, and M. j. Jin, (2020), [arXiv:2006.16145 \[hep-ph\]](#).
- [31] Z.-L. Liang, L. Zhang, P. Zhang, and F. Zheng, [JHEP **01**, 149 \(2019\)](#), [arXiv:1810.13394 \[cond-mat.mtrl-sci\]](#).

- [32] S.-F. Ge, X.-G. He, X.-D. Ma, and J. Sheng, *JHEP* **05**, 191 (2022), [arXiv:2201.11497 \[hep-ph\]](#).
- [33] C. Xia, Y.-H. Xu, and Y.-F. Zhou, *JCAP* **02**, 028 (2022), [arXiv:2111.05559 \[hep-ph\]](#).
- [34] H.-J. He, Y.-C. Wang, and J. Zheng, *JCAP* **01**, 042 (2021), [arXiv:2007.04963 \[hep-ph\]](#).
- [35] J. Guo, Y. He, J. Liu, and X.-P. Wang, *JHEP* **04**, 024 (2022), [arXiv:2111.01164 \[hep-ph\]](#).
- [36] M. Ibe, W. Nakano, Y. Shoji, and K. Suzuki, *JHEP* **03**, 194 (2018), [arXiv:1707.07258 \[hep-ph\]](#).
- [37] K. V. Berghaus, A. Esposito, R. Essig, and M. Sholapurkar, (2022), [arXiv:2210.06490 \[hep-ph\]](#).
- [38] D. Adams, D. Baxter, H. Day, R. Essig, and Y. Kahn, (2022), [arXiv:2210.04917 \[hep-ph\]](#).
- [39] G. Tomar, S. Kang, and S. Scopel, (2022), [arXiv:2210.00199 \[hep-ph\]](#).
- [40] C. Blanco, I. Harris, Y. Kahn, B. Lillard, and J. Pérez-Ríos, (2022), [arXiv:2208.09002 \[hep-ph\]](#).
- [41] H.-J. He, Y.-C. Wang, and J. Zheng, *Phys. Rev. D* **104**, 115033 (2021), [arXiv:2012.05891 \[hep-ph\]](#).
- [42] J. Kopp, J. Liu, T. R. Slatyer, X.-P. Wang, and W. Xue, *JHEP* **12**, 033 (2016), [arXiv:1609.02147 \[hep-ph\]](#).
- [43] D. Tucker-Smith and N. Weiner, *Phys. Rev. D* **64**, 043502 (2001), [arXiv:hep-ph/0101138](#).
- [44] D. Tucker-Smith and N. Weiner, *Phys. Rev. D* **72**, 063509 (2005), [arXiv:hep-ph/0402065](#).
- [45] Y. Gu, L. Wu, and B. Zhu, (2022), [arXiv:2203.06664 \[hep-ph\]](#).
- [46] G. H. Duan, K.-I. Hikasa, J. Ren, L. Wu, and J. M. Yang, *Phys. Rev. D* **98**, 015010 (2018), [arXiv:1804.05238 \[hep-ph\]](#).
- [47] M. Abdughani, L. Wu, and J. M. Yang, *Eur. Phys. J. C* **78**, 4 (2018), [arXiv:1705.09164 \[hep-ph\]](#).
- [48] M. Abdughani and L. Wu, *Eur. Phys. J. C* **80**, 233 (2020), [arXiv:1908.11350 \[hep-ph\]](#).
- [49] D. P. Finkbeiner and N. Weiner, *Phys. Rev. D* **76**, 083519 (2007), [arXiv:astro-ph/0702587](#).
- [50] C. Arina and N. Fornengo, *JHEP* **11**, 029 (2007), [arXiv:0709.4477 \[hep-ph\]](#).
- [51] S. Chang, G. D. Kribs, D. Tucker-Smith, and N. Weiner, *Phys. Rev. D* **79**, 043513 (2009), [arXiv:0807.2250 \[hep-ph\]](#).
- [52] Y. Cui, D. E. Morrissey, D. Poland, and L. Randall, *JHEP* **05**, 076 (2009), [arXiv:0901.0557 \[hep-ph\]](#).

- [53] P. J. Fox, G. D. Kribs, and T. M. P. Tait, *Phys. Rev. D* **83**, 034007 (2011), [arXiv:1011.1910 \[hep-ph\]](#).
- [54] T. Lin and D. P. Finkbeiner, *Phys. Rev. D* **83**, 083510 (2011), [arXiv:1011.3052 \[astro-ph.CO\]](#).
- [55] A. De Simone, V. Sanz, and H. P. Sato, *Phys. Rev. Lett.* **105**, 121802 (2010), [arXiv:1004.1567 \[hep-ph\]](#).
- [56] M. Freytsis and Z. Ligeti, *Phys. Rev. D* **83**, 115009 (2011), [arXiv:1012.5317 \[hep-ph\]](#).
- [57] E. D. Nobile, *The Theory of Direct Dark Matter Detection* (Springer International Publishing, 2022).
- [58] P. Agrawal, Z. Chacko, C. Kilic, and R. K. Mishra, (2010), [arXiv:1003.1912 \[hep-ph\]](#).
- [59] M. Kuhlen, N. Weiner, J. Diemand, P. Madau, B. Moore, D. Potter, J. Stadel, and M. Zemp, *JCAP* **02**, 030 (2010), [arXiv:0912.2358 \[astro-ph.GA\]](#).
- [60] C. McCabe, *Phys. Rev. D* **82**, 023530 (2010), [arXiv:1005.0579 \[hep-ph\]](#).
- [61] A. M. Green, *J. Phys. G* **44**, 084001 (2017), [arXiv:1703.10102 \[astro-ph.CO\]](#).
- [62] A. Nuñez Castiñeyra, E. Nezri, and V. Bertin, *JCAP* **12**, 043 (2019), [arXiv:1906.11674 \[astro-ph.GA\]](#).
- [63] A. K. Drukier, K. Freese, and D. N. Spergel, *Phys. Rev. D* **33**, 3495 (1986).
- [64] N. Bozorgnia, F. Calore, M. Schaller, M. Lovell, G. Bertone, C. S. Frenk, R. A. Crain, J. F. Navarro, J. Schaye, and T. Theuns, *JCAP* **05**, 024 (2016), [arXiv:1601.04707 \[astro-ph.CO\]](#).
- [65] A. Radick, A.-M. Taki, and T.-T. Yu, *JCAP* **02**, 004 (2021), [arXiv:2011.02493 \[hep-ph\]](#).
- [66] M. Vogelsberger, A. Helmi, V. Springel, S. D. M. White, J. Wang, C. S. Frenk, A. Jenkins, A. D. Ludlow, and J. F. Navarro, *Mon. Not. Roy. Astron. Soc.* **395**, 797 (2009), [arXiv:0812.0362 \[astro-ph\]](#).
- [67] M. Fairbairn and T. Schwetz, *JCAP* **01**, 037 (2009), [arXiv:0808.0704 \[hep-ph\]](#).
- [68] J. March-Russell, C. McCabe, and M. McCullough, *JHEP* **05**, 071 (2009), [arXiv:0812.1931 \[astro-ph\]](#).
- [69] Y.-Y. Mao, L. E. Strigari, R. H. Wechsler, H.-Y. Wu, and O. Hahn, *Astrophys. J.* **764**, 35 (2013), [arXiv:1210.2721 \[astro-ph.CO\]](#).
- [70] C. Tsallis, *J. Statist. Phys.* **52**, 479 (1988).
- [71] S. H. Hansen, B. Moore, M. Zemp, and J. Stadel, *JCAP* **01**, 014 (2006), [arXiv:astro-ph/0505420](#).

- [72] F. S. Ling, E. Nezri, E. Athanassoula, and R. Teyssier, *JCAP* **02**, 012 (2010), [arXiv:0909.2028 \[astro-ph.GA\]](#).
- [73] Y.-Y. Mao, L. E. Strigari, and R. H. Wechsler, *Phys. Rev. D* **89**, 063513 (2014), [arXiv:1304.6401 \[astro-ph.CO\]](#).
- [74] H.-Y. Wu, O. Hahn, R. H. Wechsler, Y.-Y. Mao, and P. S. Behroozi, *Astrophys. J.* **763**, 70 (2013), [arXiv:1209.3309 \[astro-ph.CO\]](#).
- [75] A. Klypin, S. Trujillo-Gomez, and J. Primack, *Astrophys. J.* **740**, 102 (2011), [arXiv:1002.3660 \[astro-ph.CO\]](#).
- [76] J. Guedes, S. Callegari, P. Madau, and L. Mayer, *Astrophys. J.* **742**, 76 (2011), [arXiv:1103.6030 \[astro-ph.CO\]](#).
- [77] A.-C. Eilers, D. W. Hogg, H.-W. Rix, and M. K. Ness, *Astrophys. J.* **871**, 120 (2019), [arXiv:1810.09466 \[astro-ph.GA\]](#).
- [78] S. K. Lee, M. Lisanti, and B. R. Safdi, *JCAP* **11**, 033 (2013), [arXiv:1307.5323 \[hep-ph\]](#).
- [79] A. J. Deason, A. Fattahi, V. Belokurov, N. W. Evans, R. J. J. Grand, F. Marinacci, and R. Pakmor, *Monthly Notices of the Royal Astronomical Society* **485**, 3514 (2019).
- [80] J. R. Ellis, R. A. Flores, and J. D. Lewin, *Phys. Lett. B* **212**, 375 (1988).
- [81] J. D. Vergados, P. Quentin, and D. Strottman, *Int. J. Mod. Phys. E* **14**, 751 (2005), [arXiv:hep-ph/0310365](#).
- [82] J. Engel and P. Vogel, *Phys. Rev. D* **61**, 063503 (2000), [arXiv:hep-ph/9910409](#).
- [83] J. D. Vergados, H. Ejiri, and K. G. Savvidy, *Nucl. Phys. B* **877**, 36 (2013), [arXiv:1307.4713 \[hep-ph\]](#).
- [84] L. Baudis, G. Kessler, P. Klos, R. F. Lang, J. Menéndez, S. Reichard, and A. Schwenk, *Phys. Rev. D* **88**, 115014 (2013), [arXiv:1309.0825 \[astro-ph.CO\]](#).
- [85] C. McCabe, *JCAP* **05**, 033 (2016), [arXiv:1512.00460 \[hep-ph\]](#).
- [86] L. Vietze, P. Klos, J. Menéndez, W. C. Haxton, and A. Schwenk, *Phys. Rev. D* **91**, 043520 (2015), [arXiv:1412.6091 \[nucl-th\]](#).
- [87] J. Fan, M. Reece, and L.-T. Wang, *JCAP* **11**, 042 (2010), [arXiv:1008.1591 \[hep-ph\]](#).
- [88] A. L. Fitzpatrick, W. Haxton, E. Katz, N. Lubbers, and Y. Xu, *JCAP* **02**, 004 (2013), [arXiv:1203.3542 \[hep-ph\]](#).
- [89] A. L. Fitzpatrick, W. Haxton, E. Katz, N. Lubbers, and Y. Xu, (2012), [arXiv:1211.2818 \[hep-ph\]](#).

- [90] N. Anand, A. L. Fitzpatrick, and W. C. Haxton, *Phys. Rev. C* **89**, 065501 (2014), [arXiv:1308.6288 \[hep-ph\]](#).
- [91] Z. Liu, Y. Su, Y.-L. Sming Tsai, B. Yu, and Q. Yuan, *JHEP* **11**, 024 (2017), [arXiv:1708.04630 \[hep-ph\]](#).
- [92] P. Gondolo, S. Kang, S. Scopel, and G. Tomar, *Phys. Rev. D* **104**, 063017 (2021), [arXiv:2008.05120 \[hep-ph\]](#).
- [93] P. Gondolo, I. Jeong, S. Kang, S. Scopel, and G. Tomar, *Phys. Rev. D* **104**, 063018 (2021), [arXiv:2102.09778 \[hep-ph\]](#).
- [94] G. Barello, S. Chang, and C. A. Newby, *Phys. Rev. D* **90**, 094027 (2014), [arXiv:1409.0536 \[hep-ph\]](#).
- [95] T. Donnelly and R. Peccei, *Physics Reports* **50**, 1 (1979).
- [96] T. Donnelly and W. Haxton, *Atomic Data and Nuclear Data Tables* **23**, 103 (1979).
- [97] J. D. Walecka, *Theoretical nuclear and subnuclear physics* (World Scientific Publishing Company, 2004).
- [98] R. Essig, J. Pradler, M. Sholapurkar, and T.-T. Yu, *Phys. Rev. Lett.* **124**, 021801 (2020), [arXiv:1908.10881 \[hep-ph\]](#).
- [99] D. Baxter, Y. Kahn, and G. Krnjaic, *Phys. Rev. D* **101**, 076014 (2020), [arXiv:1908.00012 \[hep-ph\]](#).
- [100] R. Essig, A. Manalaysay, J. Mardon, P. Sorensen, and T. Volansky, *Phys. Rev. Lett.* **109**, 021301 (2012), [arXiv:1206.2644 \[astro-ph.CO\]](#).
- [101] C. E. Dahl, *The physics of background discrimination in liquid xenon, and first results from Xenon10 in the hunt for WIMP dark matter*, Ph.D. thesis, Princeton U. (2009).
- [102] E. Aprile *et al.* (XENON100), *Phys. Rev. Lett.* **107**, 131302 (2011), [arXiv:1104.2549 \[astro-ph.CO\]](#).
- [103] G. Cowan, K. Cranmer, E. Gross, and O. Vitells, *Eur. Phys. J. C* **71**, 1554 (2011), [Erratum: *Eur.Phys.J.C* 73, 2501 (2013)], [arXiv:1007.1727 \[physics.data-an\]](#).
- [104] D. S. Akerib *et al.* (LZ), *Nucl. Instrum. Meth. A* **953**, 163047 (2020), [arXiv:1910.09124 \[physics.ins-det\]](#).
- [105] D. S. Akerib *et al.* (LZ), *Phys. Rev. D* **104**, 092009 (2021), [arXiv:2102.11740 \[hep-ex\]](#).
- [106] S. Knapen, J. Kozaczuk, and T. Lin, *Phys. Rev. Lett.* **127**, 081805 (2021), [arXiv:2011.09496 \[hep-ph\]](#).

- [107] M. Baryakhtar, A. Berlin, H. Liu, and N. Weiner, *JHEP* **06**, 047 (2022), [arXiv:2006.13918 \[hep-ph\]](#).
- [108] J. Bramante and N. Song, *Phys. Rev. Lett.* **125**, 161805 (2020), [arXiv:2006.14089 \[hep-ph\]](#).
- [109] K. Harigaya, Y. Nakai, and M. Suzuki, *Phys. Lett. B* **809**, 135729 (2020), [arXiv:2006.11938 \[hep-ph\]](#).
- [110] R. Catena, T. Emken, N. A. Spaldin, and W. Tarantino, *Phys. Rev. Res.* **2**, 033195 (2020), [arXiv:1912.08204 \[hep-ph\]](#).
- [111] T. Li, S. Miao, and Y.-F. Zhou, *JCAP* **03**, 032 (2015), [arXiv:1412.6220 \[hep-ph\]](#).
- [112] R. Essig, M. Fernandez-Serra, J. Mardon, A. Soto, T. Volansky, and T.-T. Yu, *JHEP* **05**, 046 (2016), [arXiv:1509.01598 \[hep-ph\]](#).
- [113] C. P. Liu, C.-P. Wu, J.-W. Chen, H.-C. Chi, M. K. Pandey, L. Singh, and H. T. Wong, (2021), [arXiv:2106.16214 \[hep-ph\]](#).